

ABSTRACT

Title of thesis: EFFECT OF MICROGRAVITY
 ON THE DEVELOPMENT AND STRUCTURE
 OF FIRE WHIRLS

Michael R. Jones
Master of Science, 2020

Thesis directed by: Dr. Michael J. Gollner
 Department of Fire Protection Engineering

Fire whirls have long fascinated the scientific community due to their unique structure and behavior. When swirl is added to a traditional diffusion flame, a dramatic intensification of combustion occurs increasing flame lengths and burning rates, producing a more vigorous state of combustion. While fire whirls have long been studied, many aspects of their behavior remain unsolved, such as the precise mechanisms by which circulation and buoyancy interact to lengthen diffusion flames in swirling flows. Microgravity presents an opportunity to directly investigate these aspects, isolating the influence of ambient circulation from buoyancy on the flame. Results are presented from tests performed at the NASA Glenn Research Center Zero Gravity Research Facilities' 5.18 s drop tower. Fire whirls were generated over a paraffin wax wick in 1 g using two offset half cylinders. A vertical bank of fans was placed at each inlet to provide continuous circulation, which was held constant throughout the microgravity drop test. Results show that the lengthening effect observed in 1 g dramatically reduces in microgravity, even under the influence of

continuous ambient circulation. Some similarities are still observed between 1 g fire whirls with strong circulation and microgravity fire whirls, with flames shrinking and expanding into a more cylindrical form. Interesting phenomena is also observed in higher-g conditions following the drop test.

EFFECT OF MICRO GRAVITY ON THE DEVELOPMENT AND
STRUCTURE OF FIRE WHIRLS

by

Michael R. Jones

Thesis submitted to the Faculty of the Graduate School of the
University of Maryland, College Park in partial fulfillment
of the requirements for the degree of
Master of Science
2020

Advisory Committee:
Professor Michael J. Gollner, Chair/Advisor
Professor Peter Sunderland
Dr. Paul Ferkul

© Copyright by
Michael R. Jones
2020

Acknowledgments

Thank you so much to Dr. Michael J. Gollner for giving me the opportunity to research and work on this new and exciting topic. From starting out on firebrands, to writing a thesis on microgravity fire whirl structure, I could never have done this without his guidance.

Much gratitude and respect to Ph.D. student Sriram Bharath Hariharan, who has been extraordinarily helpful to me throughout the whole thesis process and for always being available, no matter where he was. Even though he was not my advisor, it always felt as if I had an extra one.

I would also like to thank my fellow Graduate student Joey Dowling, who helped me to write the image processing code that was the basis for analyzing the data in this thesis, and for being a great friend along the way. I would like to thank all my fellow students in the graduate student department as well who made working there an absolute pleasure, including Ashlynne Orcurto, Michael Heck, and Lucas Crofton.

Thank you to Anita Stoppel, who sacrificed a lot of her short time here to collect inlet velocity data and generating the fan power to inlet velocity curve that was used to predict wind velocities at higher fan percentages.

Thank you to the department of Fire Protection Engineering, who has supported me as a TA over this past year, and to Nicole L. Hollywood, who ensured that I was supported and who made the whole graduate process much easier. I would also like to thank Dr. Arnaud Trouve for accepting me and for overseeing my

performance for the graduate program.

Thank you to the NASA Glenn Research Center in Cleveland, Ohio for facilitating the drop test that was the premise of this study. Special thanks to NASA Glenn staff Vittorio Valletta, Luke Ogorzaly, Eric Neumann, who were instrumental in designing, building, and operating the experiments and Drs. Sandra Olson and Paul Ferkul who were instrumental in the concept and execution of this experiment.

Thank you again to Dr. Paul Ferkul and to Dr. Peter Sunderland for taking the time out of their busy schedules and joining Dr. Michael J. Gollner on my defense committee.

Finally, thank you to my family and to Sydney Roston for their constant love and assurance.

Table of Contents

Acknowledgements	ii
Table of Contents	iv
List of Tables	vi
List of Figures	vii
Nomenclature	x
1 Introduction	1
1.1 Motivation and Objective	2
2 Literature Review	4
2.1 Fire Whirls	4
2.1.1 Natural Fire Whirl Formation	4
2.1.2 Fire Whirls in the Laboratory	7
2.1.3 Fuels	9
2.2 Fire Whirl Scaling	11
2.3 The Blue Whirl	17
2.4 Microgravity Experimentation	17
2.4.1 Methods	18
2.4.2 Microgravity Flames	20
3 Experimental Methods	21
3.1 Apparatus	21
3.2 Test Methodology	23
3.3 Video Analysis	26
3.4 Post-Drop Setup Experimentation	32
4 Results	36
4.1 Fan Velocity Calibration	36
4.2 Visual Aspects of the Fire Whirl	41
4.3 Flame Height and Width	44
4.4 Averaged Flame Height and Width	48
4.5 Fire Whirl Rotation Analysis	53

5	Discussion and Conclusions	58
5.1	Discussion	58
5.2	Conclusions	61
5.3	Future Work	62
	Bibliography	64

List of Tables

3.1	Drop tower test conditions.	25
3.2	Inlet velocity conditions measured by NASA. The green boxes represent conditions that were completed. Red indicates incomplete tests. . .	34
4.1	Fan power vs. velocity measured at NASA Glenn at different heights. Note the - marks signify conditions that were not tested.	37
4.2	Voltages and lab generated inlet velocities corresponding to NASA data.	37
4.3	All calculated inlet velocities from the Maryland apparatus corresponding to their fan percentages.	40
4.4	Averaged flame heights for all tests with the same gap size of 0.953 cm.	50
4.5	Averaged flame widths for all tests with the same gap size of 0.953 cm.	50
4.6	Averaged heights for all tests with the same fan power of 5%.	51
4.7	Averaged heights for all tests with the same fan power of 5%.	51
4.8	Each test and their respective rotation speeds.	54

List of Figures

1.1	An example of a straight inclined fire whirl viewed in California, from [1].	3
2.1	An example of a fluid sink in a vortex pattern pulling in a nearby fire and creating a natural fire whirl, from [2]. In this scenario an L-shaped fire is used in a crosswind to generate the vorticity necessary for fire whirl formation.	5
2.2	Detailed view of how air entrainment mixes with flames to generate fire whirls, from [3].	6
2.3	Two different configurations used to generate fire whirls in the laboratory.	8
2.4	Top view of Byram and Martin’s fire whirlwind apparatus from [4].	8
2.5	Different laboratory fire whirl setups. Figure b is a fixed frame setup using four walls instead of half-cylinders from [3].	9
2.6	Top view of a fire whirl setup using 12 fins to generate the vortex, similar to Figure 2.5 b, but with more fins/walls, from [5].	10
2.7	1/1000th model of the mass fires resulting from the Great Kanto Earthquake from [2]. Six fire whirls were observed, and each fire whirl type occurred.	13
2.8	Dimensionless flame height against dimensionless circulation from [2]. Data was taken from [6].	15
2.9	Map of fire whirl regimes from \dot{Q}^* vs. Γ^* (left) and \dot{Q}_D^*/S^* vs. Γ_{D^*} (right) from [7].	16
2.10	An approximately 2.5 cm wide blue whirl from [7].	18
2.11	NASA KC-135A aircraft flight path during a microgravity testing flight from [8].	18
3.1	Fans configuration on the apparatus sitting inside of the open experiment vehicle.	22
3.2	Coiled copper wire on top of the paraffin wax fuel.	22
3.3	Top-down view of the fire whirl apparatus.	24
3.4	Side view of the fire whirl apparatus.	24
3.5	Schematic of the fire whirl apparatus.	25

3.6	The first frame of Test 1 before pixel editing.	27
3.7	The first frame of Test 1 after grayscale and saturation adjustment.	28
3.8	Approximate location of the flame tip for frame 250 during test 6.	29
3.9	Approximate analysis of flame width for frame 250 during test 6.	30
3.10	Example of a prominent flame shape being manually tracked for frame 460 of test 9.	32
3.11	Top view of the enclosure with detailed measurement locations.	35
4.1	Lab fan controller voltage related to measured inlet velocity measured within the Maryland apparatus.	38
4.2	Lab fan controller voltage related to fan power, where voltage points, and therefore measured inlet velocity, were related as closely as possible to NASA measurements.	38
4.3	Best fit equation and region of the first regime.	39
4.4	Best fit equation and region of the second regime.	39
4.5	Montage of selected frames from Test 1 with about 0.25 seconds between each frame.	41
4.6	Montage of 15 frames from Test 1 with about 0.50 seconds between each frame.	42
4.7	Comparison of 1- <i>g</i> to 0- <i>g</i> fire whirl structure in Test 1.	43
4.8	Partial blue whirl formed at the end of Test 4. Occurred when the experiment vehicle reached the bottom of the drop and experienced high <i>g</i> -force.	43
4.9	Raw height and width data for Test 1. 5% fan power, 0.476 cm gap, 1.86 m/s.	44
4.10	Raw height and width data for Test 2. 5% fan, 0.318 cm gap, 1.86 m/s.	45
4.11	Raw height and width data for Test 4. 10% fan, 0.953 cm gap, 2.66 m/s.	45
4.12	Raw height and width data for Test 5. 30% fan, 0.953 cm gap, 4.69 m/s.	46
4.13	Raw height and width data for Test 6. 0% fan, 0.953 cm gap, No forced entrainment.	46
4.14	Raw height and width data for Test 7. 5% fan, 0.953 cm gap, 1.86 m/s.	47
4.15	Raw height and width data for Test 9. 1% fan, 0.953 cm gap, 0.918 m/s.	47
4.16	1- <i>g</i> and 0- <i>g</i> flame heights (a) and flame widths (b) for a constant inlet gap size of 0.953 cm.	49
4.17	1- <i>g</i> and 0- <i>g</i> flame heights (a) and flame widths (b) for a constant fan power of 5%.	50
4.18	1- <i>g</i> and 0- <i>g</i> flame heights for a constant gap size of 0.953 cm over time for a moving average of 40.	53
4.19	1- <i>g</i> and 0- <i>g</i> flame heights for a constant gap size of 0.953 cm over time for a moving average of 40.	54

4.20	1- <i>g</i> and 0- <i>g</i> flame heights for a constant fan power of 5% over time for a moving average of 20.	55
4.21	1- <i>g</i> and 0- <i>g</i> flame widths for a constant fan power of 5% over time for a moving average of 20.	56
4.22	Length and width over time for Test 4 over a moving average of 40.	56
4.23	Fan power percentage plotted against fire whirl rotation speed. Every point presented is a test condition with a gap size of 0.953 cm.	57
4.24	Inlet velocity plotted against fire whirl rotation speed. Every point presented is a test condition with a gap size of 0.953 cm.	57

Nomenclature

c	Specific heat
D_c	Characteristic length between half cylinders
Fr	Froude number
g	Acceleration due to gravity
H	Flame height
L	Horizontal length scale
p_0	Ambient air density
Δp	Change in air density at flame temperature and ambient air density
\dot{Q}	Heat-release rate
q	Heat generated per unit burning area per unit time
R	Radius of vortex core
S	Enclosure length scale
T_0	Ambient temperature
ΔT	Change in flame temperature and ambient temperature
U_b	Buoyant velocity at flame tip
U_r	Critical wind velocity
U_r	Radial velocity
U_z	Axial velocity
$U_{\theta,max}$	Maximum azimuthal velocity

$U_{\theta,\infty}$ Ambient azimuthal velocity

δ_r Radial boundary layer

Γ Circulation

Chapter 1: Introduction

Fire whirls are a unique naturally occurring phenomenon that have long been an area of interest to fire researchers. Fire whirls share many of their characteristics with other vortex phenomena such as whirlwinds, but remain distinct in their source of buoyancy, fuel combusting properties, structure, and formation patterns [3]. They occur when a fire and wind interact under the right conditions to form a vortex, creating what has colloquially been referred to as a fire tornado, which extends the flame to become substantially taller and more slender. A vortex can be simply described as a rotating region of fluid, air being the most appropriate fluid for fire whirl generation. Fire whirls entrain air through buoyancy, which causes hotter, less dense gas particles to rise, creating a pressure minimum near the whirl base.

These fires are known to be quite dangerous and, while they often only naturally linger for a few minutes, they can cause significant destruction by spreading fires and incinerating anything in their unpredictable path [9]. In 1923, Tokyo experienced a massive earthquake that resulted in a city-sized firestorm and an intense fire whirl that killed 38,000 people within 15 minutes [10]. During World War II, fire whirls were produced from the bombing of Hamburg in 1943, which resulted in the first accounts of research of these strange fire occurrences in nature [11]. While fire

whirls have long been observed in wildfires [12], Byram designed a fixed-frame fire whirl apparatus for laboratory study in 1962, the first case of fire whirls reported to be studied in a laboratory [4].

1.1 Motivation and Objective

Due to their higher temperature, enhanced burning rate, and elongated shape, fire whirls have been suggested to be a more efficient method of burning, facilitating cleaner combustion for various open-burning applications. As such, utilizing fire whirls as a tool for combustion, rather than a natural hazard, has become a recent research topic. One example is using fire whirls for more efficient oil spill cleanup. A fire whirl structure has a much longer flame sheet than its generic fire counterpart. This elongated sheet increases the surface area of the fire available for fuel combustion, producing much lower concentrations of particulates and some harmful gases. Before next steps towards this goal can be made, there is still much to be understood regarding the science of fire whirls, such as the roles circulation and buoyancy play on their formation and structure.

It has long been debated whether circulation or buoyancy is the dominating force in fire whirl structure, with the leading theory that buoyancy is the controlling factor rather than high levels of circulation, meaning that as long as enough buoyancy is supplied to a fire whirl, the amount of circulation applied is not as important in retaining fire whirl structure. Interestingly, straight inclined fire whirls have been viewed in the natural environment despite this theory, as a buoyancy-dominated fire

whirl would be expected to incline upwards due to the effects of gravity [1]. Figure 1.1 presents a snapshot of a straight fire whirl on a 30 degree slope.



Figure 1.1: An example of a straight inclined fire whirl viewed in California, from [1].

This work attempts to expand our knowledge on this topic by placing a fire whirl in an environment where buoyancy is not present and various levels of circulation are imposed. The resulting flames are analyzed for changes in geometry and flame rotation rates, and preliminary comments on scaling these effects are presented.

Chapter 2: Literature Review

This chapter provides a general background on fire whirls and their structure, as well as the forces involved in creating and sustaining them. A more detailed review of fire whirls is given in [3].

2.1 Fire Whirls

This section will include details of fire whirl formation in both natural and laboratory settings, as well as the different fuels that may be used in fire whirl experimentation. A closer look at how large fire whirls are scaled down for testing is also included.

2.1.1 Natural Fire Whirl Formation

Fire whirls form as a result of interactions between swirling flow fields and intense buoyancy, leading to an intensification of combustion with whirling flames [3]. In the natural environment, fire whirls form in large urban and wildland fires when winds interact with obstacles or natural features in the terrain [5].

For a fire whirl to form, three conditions need to be met. These conditions include a generating eddy, a fluid sink, and some friction or drag on the ground [13].

A fluid eddy can be described as a vortex, which is known as a rotating region of fluid [14].

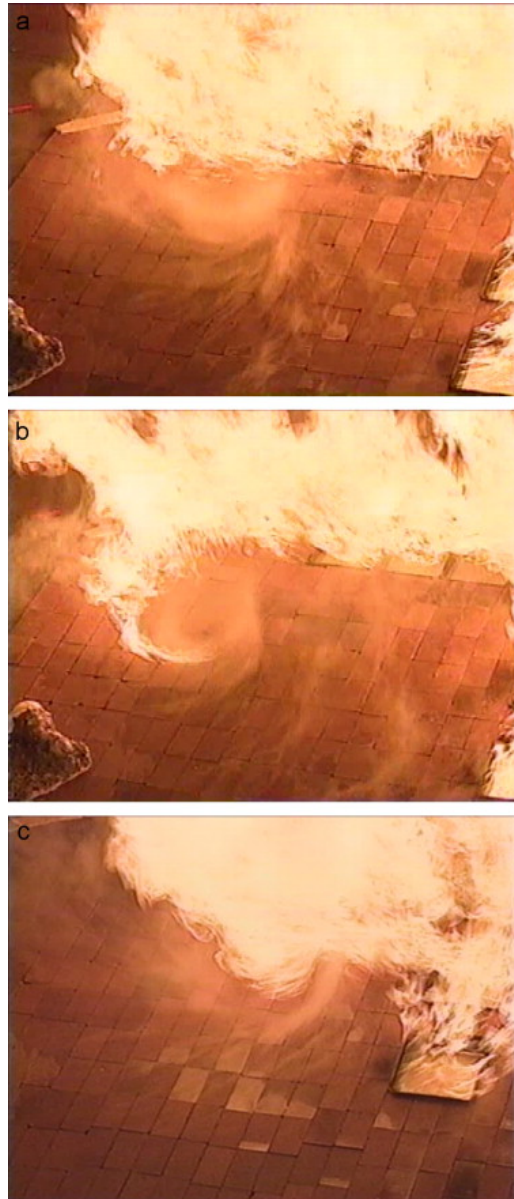


Figure 2.1: An example of a fluid sink in a vortex pattern pulling in a nearby fire and creating a natural fire whirl, from [2]. In this scenario an L-shaped fire is used in a crosswind to generate the vorticity necessary for fire whirl formation.

An example of this process can be seen in Figure 2.1. The fluid sink is created through the buoyant lifting of hot gas into the fire plume, thereby forcing air en-

trainment from the sides, as the change in density is proportional to the change in temperature [1]. This air entrainment is generated from the rising hot gases, which creates a pressure minimum on the ground, pulling in surrounding air [15]. Surface shear along the ground can be generated when air flow passes over the fire whirl generating surface, whether this be the ground in a natural environment or in an experimental laboratory setup.

Figure 2.2 presents a diagram representing the flow field surrounding a fire whirl. U_z represents the axial velocity, $U_{\theta,max}$ the maximum azimuthal velocity, U_r the radial velocity, and $U_{\theta,\infty}$ the ambient azimuthal velocity. Air can be seen flowing both around and into the flame structure, with the highest velocities found moving upwards at the center, propelled by hot gases at the center of the flame.

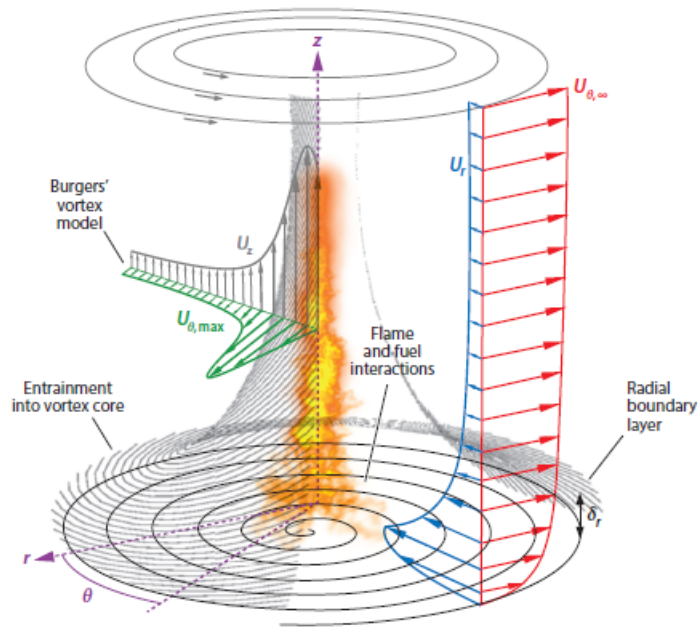


Figure 2.2: Detailed view of how air entrainment mixes with flames to generate fire whirls, from [3].

δ_r represents the thickness of the radial boundary layer, which is an essential

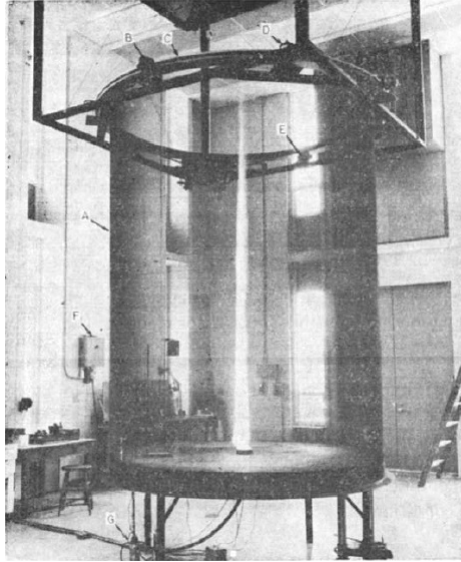
component in keeping the balance between circulation, pressure gradient, and drag within the boundary layer to deliver a radial inflow, or flow velocity towards the fire whirl [3].

2.1.2 Fire Whirls in the Laboratory

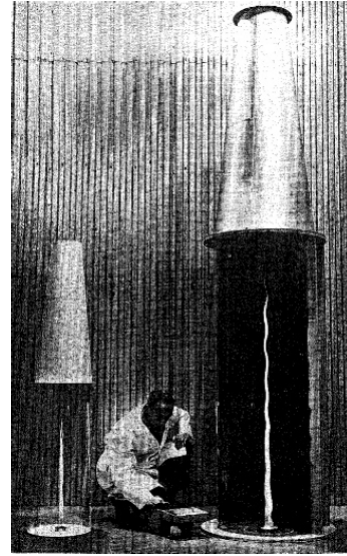
Flames created in the laboratory usually begin as pool fires, simply created by igniting a pool of liquid fuel and allowing the flames to react naturally without disruption. When tangential forced or natural air entrainment is added in the right proportions these fires transition into fire whirls. The introduced swirl condenses the central core of the vortex, drawing flame sheet closer to the surface of the pool and lengthening the flame. This modified structure results in an increased burning rate [15].

To generate fire whirls, a number of methods can be used to introduce swirl, including rotating screens and fixed frame configurations [16]. These configurations can look very different from each other, but follow the same pattern in that they force air entrainment in a circular pattern generating the vorticity necessary to form a fire whirl.

Figure 2.3 presents two early fire whirl generating apparatus used in laboratories. First, an Emmons-type apparatus forms fire whirls via rotation of a mesh screen surrounding a central fire (Figure 2.3, left) while another common method is to allow air entrainment into an apparatus only through tangential slits or vanes, slightly modified in Figure 2.3 (right) with a single inlet at the base of the setup. Al-



(a) Rotating screen fire whirl apparatus from Emmons and Ying [17].



(b) Two similar fixed frame fire whirl apparatus from Byram and Martin [4].

Figure 2.3: Two different configurations used to generate fire whirls in the laboratory.

though the configurations use different methods to impose vorticity, air is ultimately entrained in similar patterns. Figure 2.4 gives a clearer top view of 2.3(b).

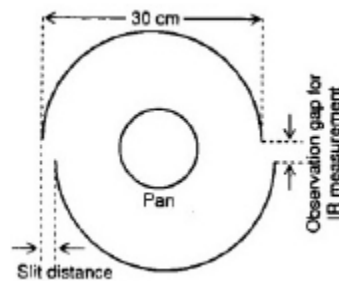


Figure 2.4: Top view of Byram and Martin's fire whirlwind apparatus from [4].

Available fixed-frame configurations for fire whirl formation are summarized in Figure 2.5 with (c) and (d) representing the previously-described apparatus of Byram and Martin and Emmons and Ying, respectively. Finally, configurations in Figure 2.5 (a) and (b) include two or more slits that allow tangential air entrainment.

They can even be arranged with more than four walls, then often calling these obstructions fins, seen in Figure 2.6.

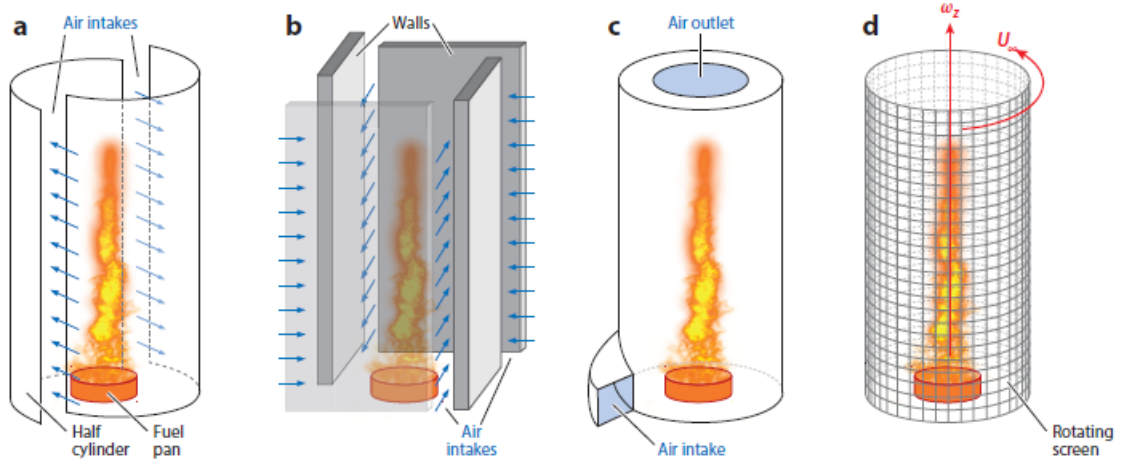


Figure 2.5: Different laboratory fire whirl setups. Figure b is a fixed frame setup using four walls instead of half-cylinders from [3].

2.1.3 Fuels

Many fuel types are used in fire whirl experimentation. Gas, liquid, and solid fuels can all be used to study fire whirl behavior, each with their own benefits and drawbacks. Generally, changing fuel types can be useful to further understand fire whirl phenomena, such as interchanging gaseous and liquid fuels to understand controlling parameters affecting flame height [18] or different liquid fuels to understand the structure of the blue whirl [19].

Generally, fuels for fire whirl experiments can be either fed into the apparatus or placed at the center of the enclosure for a specified burning duration. If a solid fuel is used, it must be placed before ignition. If a gaseous fuel is used, it must be fed into the enclosure. If a liquid fuel is used, it can either be poured into an

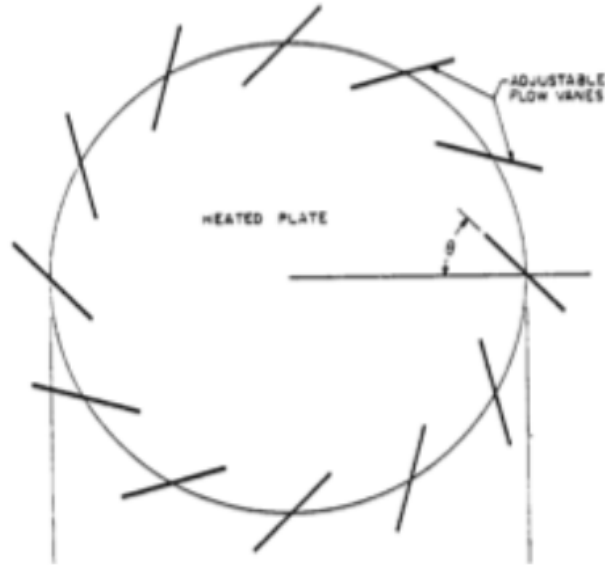


Figure 2.6: Top view of a fire whirl setup using 12 fins to generate the vortex, similar to Figure 2.5 b, but with more fins/walls, from [5].

enclosure pan or fed in like a gas. When poured into an enclosure pan, it is common to pour cold water into the pan and then fill up the rest of the pan area with fuel until it reaches the rim [2]. This is to ensure that the fuel level is level with the pan rim and therefore the enclosure base, which is necessary to keep the base smooth. Pouring in colder water before the fuel helps to keep the bulk of both fluids below their boiling temperature for a longer period, avoiding boil-over which results in vigorous combustion not desirable for most experiments.

Lei et. al built an experimental apparatus with the ability to feed in propane gas and control the flow with a flow meter [20]. Chauh et al. used a fuel pan for inclined fire whirl experiments, interchanging methanol, ethanol, and 2-propanol, containing the liquid to the pan using small aluminum slits that prevented the fuel from spilling out [1]. Solid fuels are also valid fuel sources for fire whirl experimentation. Paraffin wax and other ignitable solids can be used.

2.2 Fire Whirl Scaling

Because of the inherent safety concerns related to fire whirls, generating them at large scale is exceedingly difficult. Scaling therefore arises as a method of re-creating large-scale phenomena at smaller scales by keeping in mind appropriate physical parameters. The process of fire whirl scaling is therefore typically used to re-create fire whirls seen in nature within a laboratory environment. Most laboratory fire whirl experiments are generated using the fixed-frame methods previously mentioned, although the formation mechanisms of urban and forest fire whirls are not well studied [2]. Researchers have conducted experiments of fire whirls under the influence of lateral winds, noting that these have aided in the generation of fire whirls under the right conditions [2]. Graham first hypothesized that most forest fire whirlwinds occurred within a certain range of wind velocity, and stressed the importance of lateral winds in fire whirl formation [21]. Soma and Saito later suggested that the interaction of mass fires along with relatively calm lateral winds of around 4 to 5 m/s led to the generation of most intense fire whirls. They conducted a series of scale-model experiments and found a narrow range of lateral wind velocity that led to fire whirl generation [22]. It was found that the heat-release rate was also a critical parameter, being tied to the wind speed. They concluded that the occurrence of open-space fire whirls could be predicted by considering the burning area as an obstruction to the flow and determining the critical wind speed, or the wind speed that affects fire whirls most strongly, is proportional to the vertical buoyant velocity. The critical wind speed then also depends on the burning rate as well as

the length scale of the burning area [23].

Kuwana et. al. developed a 1/1000th scale model of a large fire whirl that damaged Tokyo after the Great Kanto Earthquake in 1921 within a large-scale wind tunnel. Figure 2.7 presents the layout of the heptane fuel pans representing the burning area of the model, which are surrounded with bricks to keep the fuel surface level with the surroundings. With a run duration of approximately 2 min, 16 runs were conducted. The lateral wind velocity was varied from 0.5 m/s to 2 m/s, but it was ultimately determined that the critical wind velocity for the experiment was 1 m/s, which scaled up to around 4 to 5 m/s in a full-size fire whirl, as a wind velocity of 0.5 m/s produced very weak whirls and a wind speed of 2 m/s tilted the flames downstream too far for many fire whirls to form. Three types of fire whirls were formed, each occasionally seen in the natural environment. The first type appeared to be a tall fire column, which extended a non fire whirl flame height from 1 to 5 m. The second type was a short-lasting fire whirl that resembles fire whirls often seen in forest fires. The last type resembled the large open-space fire whirl that devastated Tokyo in 1921 [2].

Several parameters were considered to predict the critical lateral wind velocity at which the strongest fire whirl was generated, shown in Equation 2.1 [2].

$$U_c = \varphi(c, L, q, \rho_0, \Delta\rho, T_0, \Delta T, g) \quad (2.1)$$

These parameters include c , the specific heat of air, L , the horizontal length scale of the burning area, q , the heat generated per unit burning area per unit time, ρ_0 ,

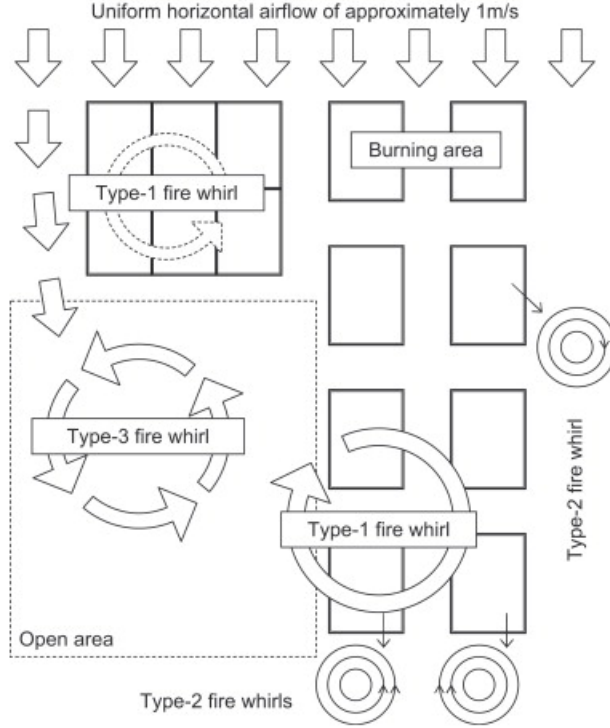


Figure 2.7: 1/1000th model of the mass fires resulting from the Great Kanto Earthquake from [2]. Six fire whirls were observed, and each fire whirl type occurred.

the ambient air density, $\Delta\rho$, the difference between air density at the temperature of the flame and the ambient air density, T_0 , the ambient temperature, ΔT , the difference between the flame temperature and the ambient temperature, and finally g , the acceleration due to gravity.

Equation 2.2 presents the application of the Buckingham Pi theorem for dimensional analysis to Equation 2.1 [2].

$$U_c/(gL)^{1/2} = \Phi'(\Delta\rho/\rho_0, \Delta T/T_0, q/(c\rho_0\Delta T(gL)^{1/2})) = \Phi'(\Pi_1, \Pi_2, \Pi_3) \quad (2.2)$$

In regards to the critical wind velocity, it was determined that for fires with a horizontal length scale as small as 1 m to over 1 km, the ratio of lateral wind velocity

and buoyant velocity at the flame tip is constant, or that they are proportional to each other [2]. This was determined from the well-established correlation $H/L \sim Fr^n$, where H is the flame height, $1/5 < n < 1/3$, and Fr is the Froude number [24], as well the relationship $U_b \sim (gH)^{1/2}$, where U_b is the buoyant velocity at the flame tip [25].

The flame height was determined to be a factor of the same variables as the critical wind velocity, but also including R , the radius of the fire whirl vortex core and Γ , the circulation, as shown in Equation 2.3 [2].

$$H = \varphi(c, L, q, p_0, \Delta p, T_0, \Delta T, g, R, \Gamma) \quad (2.3)$$

Equation 2.4 presents the application of the Buckingham Pi theorem of dimensional analysis to Equation 2.3 [2].

$$H/L = \Phi'(\Delta\rho/\rho_0, \Delta T/T_0, q/(c\rho_0\Delta T(gL)^{1/2}), R/L, \Gamma^2/(gL^3)) = \Phi'(\Pi_1, \Pi_2, \Pi_3, \Pi_4, \Pi_5) \quad (2.4)$$

In cases in which Γ is much greater than $(gL^3)^{1/2}$, Π_5 is anticipated to be the dominating dimensionless number, where only its effects must be considered, which is affected by Γ , g , and L . This is because Π_1 and Π_2 are nearly constant for ordinary fires, Π_4 is a parameter of order unity, and Π_3 becomes much smaller than Π_5 . In this case, Equation 2.4 can be rewritten as Equation 2.5 based on a fit of

their experimental data, shown below [2].

$$H/L \sim (\Gamma^2/(gL^3))^{1/3} \quad (2.5)$$

As $\Gamma^2/(gL^3)$ approaches infinity, a scaling relationship with H/L is observed, shown in Figure 2.8.

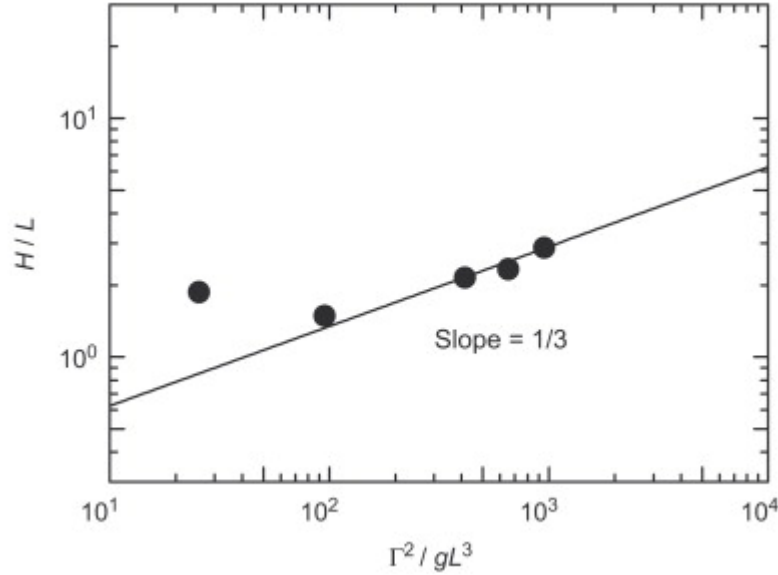


Figure 2.8: Dimensionless flame height against dimensionless circulation from [2]. Data was taken from [6].

Hu et al. created a different scaling law based off of their fixed offset cylinder setup where the gap size and the volumetric fuel flow rate was varied, which was used to control the heat-release rate, \dot{Q} , and the circulation, Γ [7]. Here, Γ depends on the variables presented in Equation 2.6.

$$\Gamma = f'(\dot{Q}, S, D_c, T_0, \rho_0, \Delta T, \Delta \rho, C_{p,0}, g) \quad (2.6)$$

D_c represents the characteristic length of the enclosure between the half cylinders, $C_{p,0}$ is the specific heat of air at ambient temperature, S represents the length scale parameter, and each other variable is the same as in Equation 2.1. After applying the Buckingham Pi theorem and forming a set of non-dimensional quantities, and then neglecting variables with comparatively smaller values, Γ becomes dependent on the variables presented in Equation 2.7.

$$\Gamma_D^* = \Phi(\dot{Q}^*, S^*) \quad (2.7)$$

Here, $\Gamma_D^* = \Gamma/D_c\sqrt{gD_c}$, $\dot{Q}^* = \dot{Q}/(C_{p,0}\Delta T\rho_0D_c^2\sqrt{gD_c})$, and $S^* = S/D_c$. Figure 2.9 presents the flame regions, discussed in the next section, as well as which type of fire whirl that is formed, between the upper and lower bounds given in each graphic.

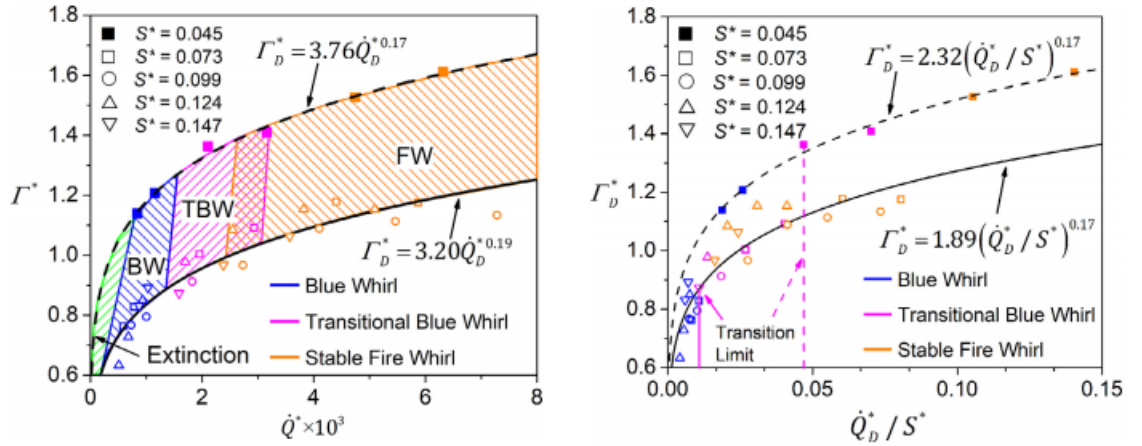


Figure 2.9: Map of fire whirl regimes from \dot{Q}^* vs. Γ^* (left) and \dot{Q}_D^*/S^* vs. Γ_D^* (right) from [7].

Hartl and Smits developed a small scale burner model that seems to reinforce the previously mentioned models. The primary non-dimensional groups were determined to be Γ^* , q^* , known as heat release, and S^* . Their results also indicate

that non-dimensional height, H^* , is only a function of Γ^* . Lastly, Hartl and Smits determined that for all data sets, the Froude number, $Fr = U_{CL}/\sqrt{gz}$, is dependent on the product of q^*S^* . As this product gets larger, Fr approaches a constant value and is consistent with buoyancy driven flow [15].

2.3 The Blue Whirl

The blue whirl is a fire whirl regime that burns liquid hydrocarbons directly with little visible soot [5] [26] [19]. The blue color arises from combustion with very little soot, with temperatures which peak around 2000 K [19] [27] [28], due to efficient mixing of evaporated fuel and air [29], shown in Figure 2.10. While it has been shown that both heat-release rate, \dot{Q} , and circulation, Γ , serves an important role in the formation of generic fire whirls [30], it is likely that these parameters also serve an important role in the formation of the blue whirl as well. Others used the relationship between these quantities and the scaling described in the previous section to determine the combinations of heat-release and circulation required to form the blue whirl and a traditional fire whirl, outlining both regions and the transition region between them in Figure 2.6 [7].

2.4 Microgravity Experimentation

The study of microgravity combustion involves the study of combustion processes in an environment where gravity is much weaker than in normal conditions. In regards to fire, this is usually performed to study flames with minimal buoyant

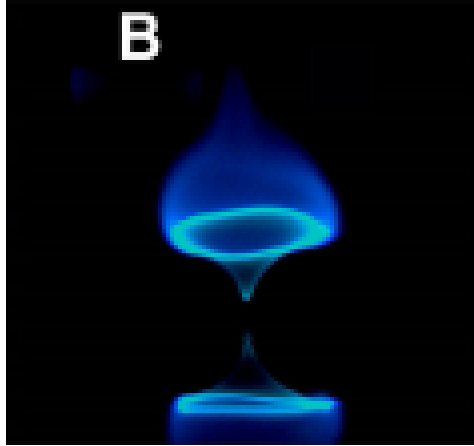


Figure 2.10: An approximately 2.5 cm wide blue whirl from [7].

effects.

2.4.1 Methods

The earliest known study of pre-mixed gaseous flames in microgravity was performed by Krivulin in 1980 when an aircraft flying at parabolic trajectories was used to study the effects of buoyancy on flammability limits [31]. A NASA aircraft capable of performing such experiments is presented in Figure 2.11.

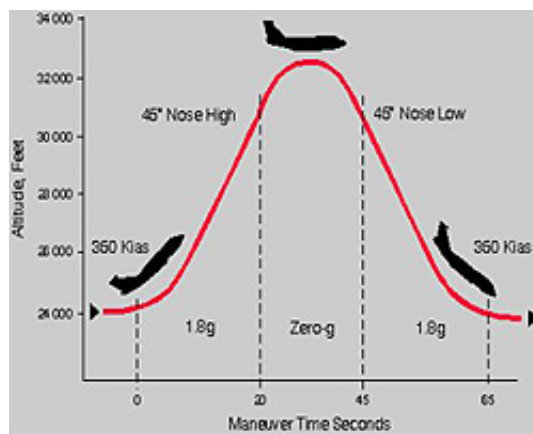


Figure 2.11: NASA KC-135A aircraft flight path during a microgravity testing flight from [8].

The aircraft achieves weightlessness by performing parabolic maneuvers. Each

flight will perform 40 to 60 of these maneuvers, which more specifically include a 45 degree incline into a short period of leveling off into a 45 degree decline. This process supplies people and experimental equipment on board with about 25 seconds of microgravity [8]. As seen in Figure 2.11, weightlessness is simulated at the peak of the parabolic curve, when the plane is transitioning ascent and descent. The biggest benefit of using this method is that it provides the experiment the longest duration of near weightlessness and is fairly stable.

The International Space Station, known as the ISS, provides researchers with a platform for long-duration microgravity experimentation. A microgravity environment is achieved on the ISS as it is in constant free fall around the Earth. As a result, there is very little buoyancy-driven convection occurring within fluid bodies during ISS experiments [32].

NASA also uses drop towers to simulate microgravity environments. Specifically, two drop towers are located at the NASA Glenn Research Center in Cleveland, Ohio. One tower offers a drop time of 2.2 seconds, the other offers a drop time of 5.18 seconds. In the 2.2 second tower, weightlessness is simulated by placing an experiment within a drag shield. This drag shield is used to isolate the experiment from drag effects associated with free-fall. The experimental package will experience a peak gravitational acceleration of 0.001 g and will fall a total of 24 meters. In the 5.18 second tower, weightlessness is simulated by pumping out all air within the zero gravity testing chamber to an internal pressure of around 6.667 pascals. This way, a drag shield is not necessary and can reduce aerodynamic drag on the free-falling vehicle to less than 0.00001 g and will fall a total of 132 meters.

2.4.2 Microgravity Flames

Buoyancy forces are the result of density differences between solids, liquids, gases, and their surroundings. In a fire environment, the plume of hot gases will naturally induce convection in the surrounding colder air, as gaseous combustion products are generally 7-10 times less dense due to higher temperatures than the unburnt reactants at standard temperature and pressure [33]. When this fire environment is moved into microgravity, buoyancy effects are lost. Rather, diffusive transport becomes the dominant mode of heat and mass transfer [33].

The goal of performing the seven drop test experiments detailed in this report is to limit the influence of buoyancy on pre-formed fire whirls. Microgravity offers a unique environment to do just this, and allows researchers the opportunity of separating formation processes for a more comprehensive understanding of fire whirls.

Chapter 3: Experimental Methods

This chapter explains the apparatus, configuration, and the processes that were involved in testing and recording data. This involves a detailed account of test methodology and the testing facility. An explanation of how data was analyzed is also given.

3.1 Apparatus

A fire whirl enclosure was first constructed at the NASA Glenn Research Center using two PMMA half-cylinders offset by a variable distance such that three different gap sizes could be analyzed. These gap sizes are later specified in the test methodology section. A vertical bank of three 60 mm by 25.4 mm fans (Delta Electronics Axial Fan 12 VDC AFB0612DH-TP11) were aligned with the gaps on either side of the enclosure at both inlets. These can be easily viewed in Figure 3.1. The fan powers were altered in each test to vary the inlet wind speed into the enclosure. These powers were varied using an Ecolicity PWM dimmer controller where an analog voltage was sent to the controller and this would generate varying PWM signals to the fans. These half-cylinders were centered on top of a 5 cm diameter paraffin wax wick, which was then ignited using a heated coiled wire along



Figure 3.1: Fans configuration on the apparatus sitting inside of the open experiment vehicle.

the top of the wick. The coiled wire can be seen in Figure 3.2.



Figure 3.2: Coiled copper wire on top of the paraffin wax fuel.

Two video cameras, each at 120 fps, were placed around the enclosure. One was placed to obtain top-views of the fire whirl structure, while the other was placed to obtain side-views. This entire enclosure was then placed into an experiment vehicle.

Figures 3.3 and 3.4 present the top and side views of the model, respectively. The yellow body represents the two offset half-cylinders. The gray pieces on either side model the fan configuration at each inlet. A schematic of the fire whirl enclosure that was placed in the stainless steel shell with camera locations can be seen in Figure 3.5. The two PMMA half-cylinders can be seen offset from each other as to allow air to be entrained in a swirling pattern, which is necessary for fire whirl formation. The two cameras are represented by the large yellow rectangles both at the top of the enclosure and to the right.

Unfortunately, there are some non-ideal aspects of the fire whirl setup imposed by the materials and restraints of the test rig. At the bottom portion of the interior, there is a small gap that allowed flow through the bottom, which required duct tape to be closed up. There was also a small gap on one of the fan controllers. Finally, due to a protrusion in the offset cylinders, the fan bank began at an offset from the bottom of the apparatus, shown in Figure 3.4. This created a small zone without tangential airflow at the base of the fire whirl, where the boundary layer entering the fire whirl has previously been found to be critical in fire whirl formation [28].

3.2 Test Methodology

The tests were conducted at the Zero Gravity Research Facility at the NASA Glenn Research Center. The chamber is 6.1 m in diameter and the air inside is pumped out until the pressure within the chamber is about 6.67 Pa. After dropping for the specified duration, the vehicle lands in a decelerator cart 3.3 m in diameter

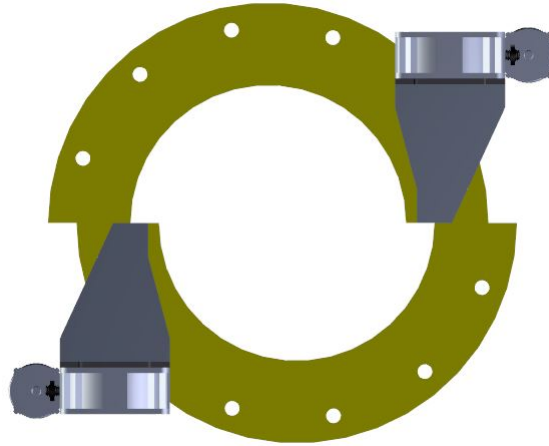


Figure 3.3: Top-down view of the fire whirl apparatus.

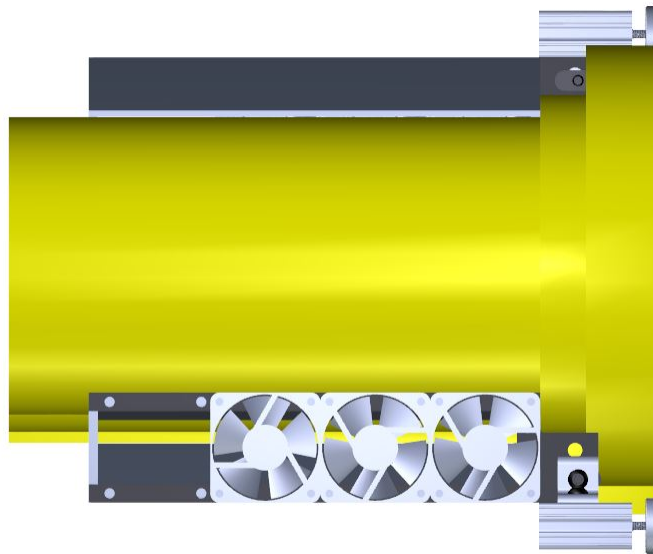


Figure 3.4: Side view of the fire whirl apparatus.

and 6.1 m deep. The cart is filled with 3 mm polystyrene beads that help dissipate the kinetic energy gained from falling over the 5.18 s duration. After each test, the experiment vehicle is retrieved, cleaned off, and prepared for the next test.

Two parameters were varied between the seven tests analyzed. These parameters are the gap size formed by the offset of the PMMA half-cylinders and the inlet

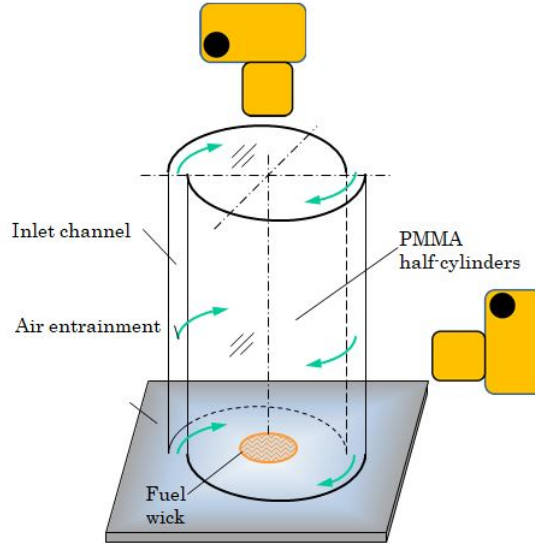


Figure 3.5: Schematic of the fire whirl apparatus.

wind speed in the form of percentage fan power. The different test conditions are as follows: 0.318 cm gap size at an inlet velocity of 5% fan power, 0.476 cm at 5% fan power, and 0.953 cm at 0%, 1%, 5%, 10%, and 30% fan power. There were three different gap size configurations at an inlet velocity of 5% fan power, as well as five different inlet velocities at a gap size of 0.953 cm. These fan powers are later converted to velocity profiles with testing in a replicate setup. These conditions are more easily understood viewing Table 3.1. It should be noted that tests 3 and 8 were discarded due to technical difficulties associated with their respective test procedures.

	Test 1	Test 2	Test 4	Test 5	Test 6	Test 7	Test 9
Gap Size [cm]	0.476	0.318	0.953	0.953	0.953	0.953	0.953
Fan Power [%]	5	5	10	30	0	5	1

Table 3.1: Drop tower test conditions.

At the beginning of each test, the coiled wire was turned on to melt and

ignite the paraffin wax. The fan powers were then adjusted to their predetermined powers until a stable fire whirl was formed. Once a stable fire whirl was achieved, burning for about 2 seconds, the hanging vehicle was dropped down the drop tower, with the two video cameras previously mentioned recording. These cameras also included time stamps in each frame, which helped to identify the exact time the vehicle transitioned into microgravity and when it landed in the polystyrene beads. The vehicle was then retrieved and prepared for the next test. Each set of test conditions was conducted only once given the limited number of tests available.

3.3 Video Analysis

The top-views and side-views of each test were extracted from the enclosure video cameras, which were fixed for each test, and analyzed. The length of the flames in each image frame were determined using a calibration image of a ruler placed in the same plane as where the flame would be located. With the line tool in ImageJ, a calibration ratio of pixel count to actual length was determined. To account for the warping of the camera lens, a length of 1 cm in pixels was measured at the far left side, the far right side, and in the middle of the image, varying by about 2 pixels on each side. These pixel counts were then averaged. This ratio was found to be 1 cm for every 57 pixels.

The flame tip and flame width were tracked in the side-view videos of each experiment using a local thresholding method in a MatLab script. First, the video being analyzed is read into MatLab using the *VideoReader* command. Then, each

frame is read using the *readFrame* command and assigned to a usable variable. Each frame in the video in question is then converted to grayscale using the MatLab command *rgb2gray*. Each frame of the video is known to have a pixel count of 1920 by 1024 pixels. Then, each frame is adjusted to increase the pixel contrast by saturating the bottom 1% and top 1% of all pixel values using the MatLab command *imadjust*. Figures 3.6 and 3.7 present the original frame and the same frame after these adjustments, respectively. Each of these adjusted frames are then stored into a large 1920 by 1080 by K matrix, where K is the amount of frames in the video. Each cell in this matrix contains a pixel's luminosity value.



Figure 3.6: The first frame of Test 1 before pixel editing.

For a pixel to be considered part of the flame, the pixel in question along

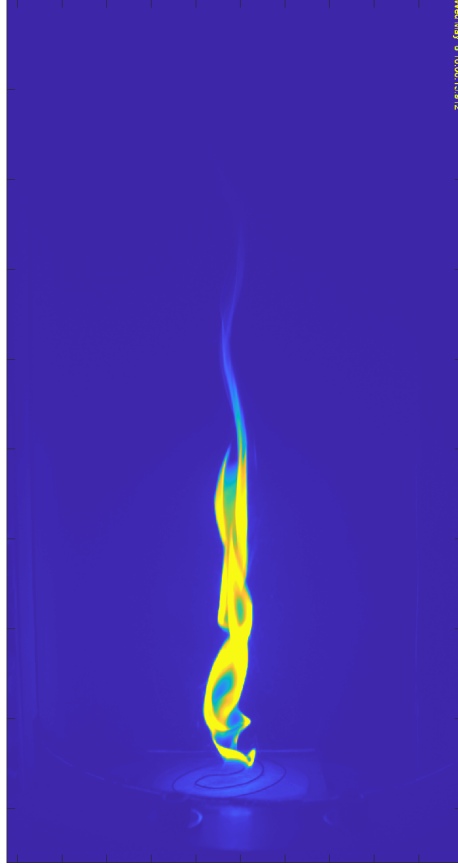


Figure 3.7: The first frame of Test 1 after grayscale and saturation adjustment.

with each of the eight pixels immediately around it would need to have a luminosity value greater than 50 on an 8-bit grayscale. The script would begin by searching the leftmost column of pixels of each frame where a flame was present, starting with the first frame of the video. The script would begin with the top of the frame and then finish searching at the bottom. If no flame was found in this column, the script would search the next column of pixels and continue to do so until the column with the flame tip was found. This value was then subtracted from the predetermined base of the flame, or 1720 pixels to the right of the leftmost column of pixels, to determine the overall flame length per frame. An example of this methodology is presented in Figure 3.8. The flame tip is marked with a red dot, which was also

used to verify the accuracy of the script by having the capability to singularly check multiple frames throughout each test video.

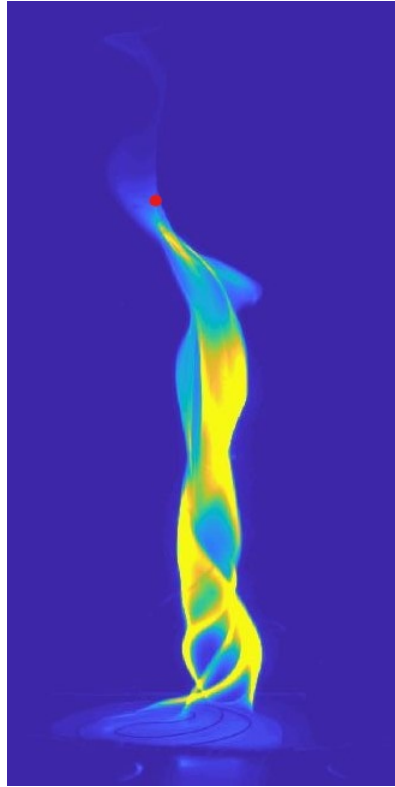


Figure 3.8: Approximate location of the flame tip for frame 250 during test 6.

Two separate matrices were created to store the length and width values taken for each frame of each video. For length, this is a K by 4 matrix, where K is the number of frames in the video being analyzed. The fourth column of this length matrix calculates the time passed using the *FrameRate* command. The time is calculated by dividing the frame's numerical value by the video frame rate. The first column is the actual flame length in cm, and the second and third columns are the y-coordinate and x-coordinate of the flame tip, respectively.

Width was then tracked by utilizing this same method starting from the flame tip, but worked by locating the first and last instances where the pixel in question

and the eight pixels around it satisfied the threshold condition. This method was utilized in each column of the frame from the flame tip to the predetermined base. The flame width and height could be tracked for each video with time for each experiment. Figure 3.9 represents the same frame as Figure 3.8, but with added red dots outlining the width of the flame. Flame width was averaged per frame by averaging all flame width values from the flame tip to the flame base, and then averaged again over the entire video so that change in frame-averaged flame width could be tracked over time.

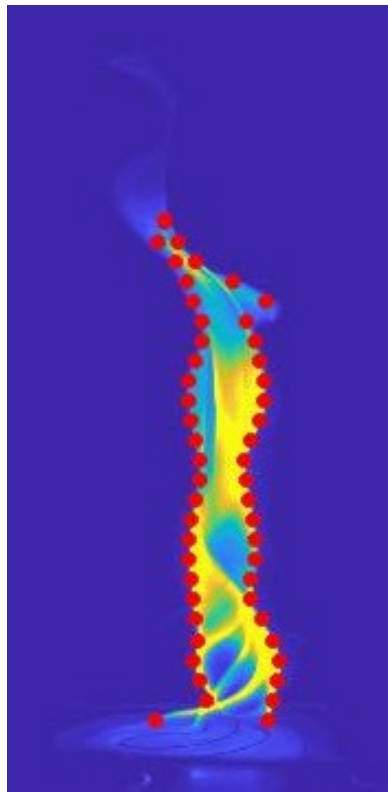


Figure 3.9: Approximate analysis of flame width for frame 250 during test 6.

The width matrix previously mentioned is a 5 by J by K matrix, where J is the calculated number of pixel columns between the flame tip and the flame base at 1720 pixels, and K is the number of frames being analyzed. The first row of

the matrix stores the x-coordinate value, which indicates which column of pixels in the frame the width is being calculated. The second and third rows are the two y-coordinates, the top of the flame being the second matrix row and the bottom of the flame being the third row. The fourth row is just the second row subtracted from the third, giving the actual flame width in pixels. Lastly, the fifth row is the fourth row divided by 57 pixels, giving the actual column flame width in cm.

To paint the red dots back over the image, which was used to verify the accuracy of the code, the MatLab command *linspace* was used. This was used to create two vectors, one along the x-axis of the frame and one along the y-axis. These vectors were the same lengths as the resolution of each frame. The *image* command was then used to overlay these vectors on top of the frame of the video. Lastly, *plot* was used to paste the red dots in their proper locations. These dots are actually pasted within the *linspace*, but look like they are pasted onto the image due to their layering.

Tangential fire whirl rotation speeds were calculated using Spotlight-16, where specific flame features visible in the fire whirl from the top-down view were tracked manually frame-by-frame, giving a measure of the distance traversed by the flame feature in a time period determined by the number of frames that the feature was visible. This was done by creating an Area Of Interest (AOI) and then using the manual tracking tool to select a point on the flame, which would then progress the image sequence to the next frame. This process was completed over as many frames as possible before the tracked feature disappeared. These rotation speeds were tracked over a small enough duration that the flame precession was unable to

make a large enough impact in the recorded measurements. Figure 3.10 presents a still example of this process.



Figure 3.10: Example of a prominent flame shape being manually tracked for frame 460 of test 9.

3.4 Post-Drop Setup Experimentation

After the drop tests were completed, similar replicates of the half-cylinder shells used in the drop tests were acquired and more $1g$ tests were conducted. The inlet wind speed values were non-ideally relayed in terms of fan power percentage.

Due to this situation, actual inlet wind velocities were left unknown. To remedy this issue, NASA researchers conducted wind velocity measurements at specific fan powers and at different heights along the enclosure inlets with a wind measuring device. Table 3.2 presents the different test conditions completed by NASA.

Figure 3.11 presents a top-down view of how NASA measured interior flow. Velocity was measured at Θ values of 5 and 45 degrees. Both s values indicate the distance from the enclosure wall that the flow was measured, which was 8.375 (+/-1) mm for both sides. The h values indicate the height above the fuel where the measurements took place.

After receiving inlet measurements, the shells were set up on top of a lab table and the fans were connected to an adjustable DC power supply. The lowest recorded value displayed on the power supply when the fans started to move was considered to be 1% fan power. A handheld hot-wire anemometer was placed in front of the fans at the same heights as displayed in Table 3.2. The knob on the controller was slowly raised until the anemometer reached similar values as the values that NASA provided. The voltages at these values were recorded. This was done for fan powers of 1%, 2%, and 5%. The methodology for finding voltages and inlet velocities for fan powers of 10% and 30% will be discussed in the following chapter.

h1,h2	Gap Size	Inlet Fan Power	Test#
3 cm	0.476 cm	5%	1
		6%	3
5 cm	0.476 cm	5%	1
		7%	3
10 cm	0.476 cm	5%	1
		7%	3
12 cm	0.476 cm	5%	1
		7%	3
3 cm	0.318 cm	5%	2
5 cm	0.318 cm	5%	2
10 cm	0.318 cm	5%	2
12 cm	0.318 cm	5%	2
3 cm	0.953 cm	1%	9
		2%	8
		5%	7
		10%	4
		30%	5
5 cm	0.953 cm	1%	9
		2%	8
		5%	7
		10%	4
		30%	5
10 cm	0.953 cm	1%	9
		2%	8
		5%	7
		10%	4
		30%	5
12 cm	0.953 cm	1%	9
		2%	8
		5%	7
		10%	4
		30%	5

Table 3.2: Inlet velocity conditions measured by NASA. The green boxes represent conditions that were completed. Red indicates incomplete tests.

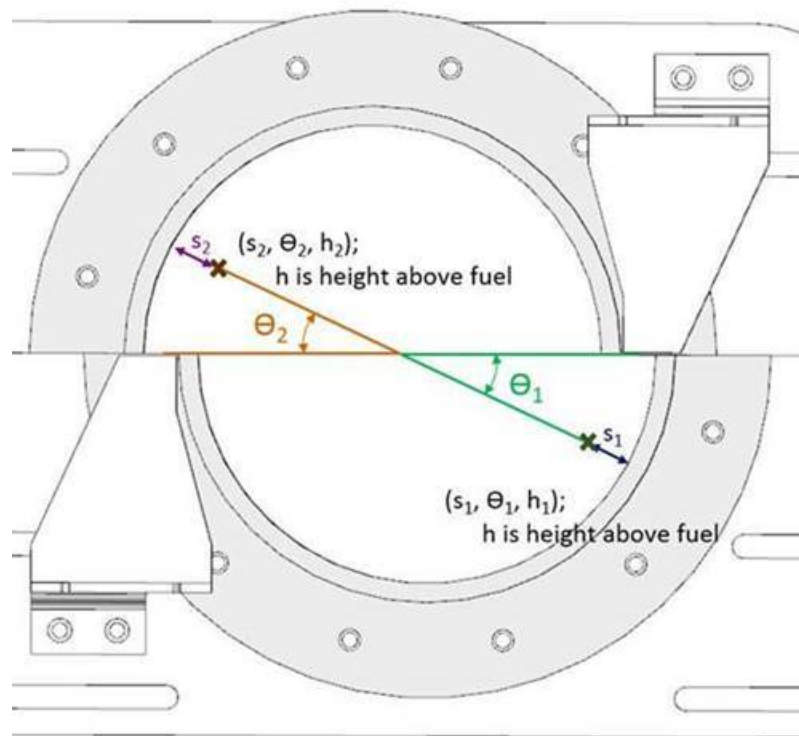


Figure 3.11: Top view of the enclosure with detailed measurement locations.

Chapter 4: Results

This chapter presents the results of the seven drop tests that were analyzed. These results include both visual and analytical changes in flame height and width over the duration of the drop as well as tangential fire whirl rotation speed based on the shell gap size and fan power conditions.

4.1 Fan Velocity Calibration

The goal of calibrating the apparatus fans is to match the NASA fan settings to the University of Maryland setup. In order to attain inlet velocities for fan powers of 10% and 30%, a curve was fitted to the limited values collected at NASA Glenn in the original test rig. When combined with the voltage values taken in the University of Maryland lab, inlet wind velocities and power supply voltages for each of the previously mentioned fan power percentage was attained.

Table 4.1 presents the anemometer measurements received from NASA. As also seen in Table 3.2, the 10% fan power setting was only measured at 5 cm above the base of the original enclosure at NASA Glenn. Using the data that was provided by NASA, fan power versus controller voltage was recorded for 1%, 2%, and 5%, and is presented in Table 4.2.

Height [cm]	NASA 1% [m/s]	NASA 2% [m/s]	NASA 5% [m/s]	NASA 10% [m/s]
3.4	0.825	1.31	2.04	-
5	0.614	0.895	1.33	2.07
10	0.834	-	2.12	-
12	0.792	1.27	2.06	-
Avg.	0.766	1.16	1.89	-

Table 4.1: Fan power vs. velocity measured at NASA Glenn at different heights. Note the - marks signify conditions that were not tested.

Fan Percentage	1%	2%	5%
Voltage [V]	4.00	4.01	4.10
Corresponding Velocity [m/s]	0.918	1.27	1.86

Table 4.2: Voltages and lab generated inlet velocities corresponding to NASA data.

To generate the voltages and therefore the corresponding inlet velocities for fan powers of 10% and 30%, a curve was fitted to the data points that were already found. One issue here is that the inlet velocity varies a large amount with height, so anemometer placement is important. When viewing the fan power to velocity data, it appears that the data follows two different linear regimes, switching once the fan controller power reaches a voltage of 4.30 V. Figure 4.1 presents this data.

In order to find the voltages associated with their fan powers, it was first necessary to determine which regime the two sought after points were in. When plotting fan controller power against fan percentage a linear trendline is created in the first regime up to about 4.3 V, expressed as $P = 37.4V - 148$, where V is voltage and P is fan power. This is shown in Figure 4.2. Plugging in a value of 10% fan power for P , it was determined that 10% is related to a controller voltage of 4.23 V, and is therefore in the first regime. Plugging in a value of 30% fan power for P , it was determined that 30% is related to a controller voltage of 4.77 V, and is therefore

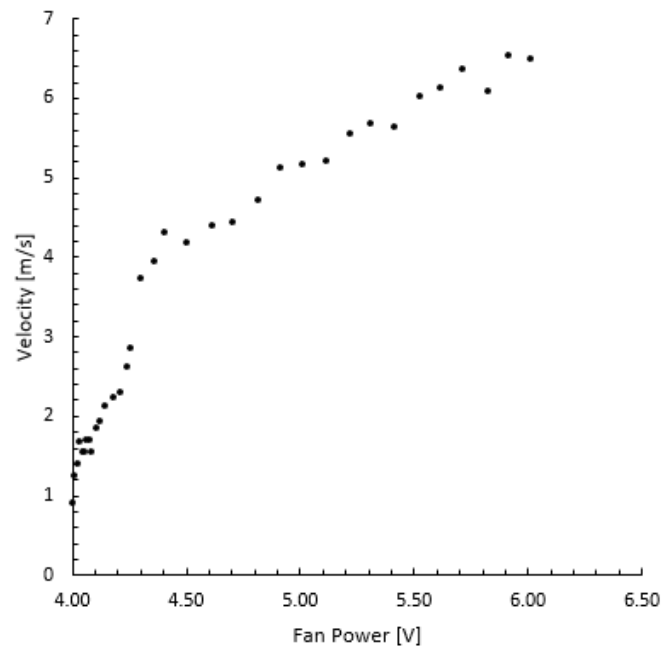


Figure 4.1: Lab fan controller voltage related to measured inlet velocity measured within the Maryland apparatus.

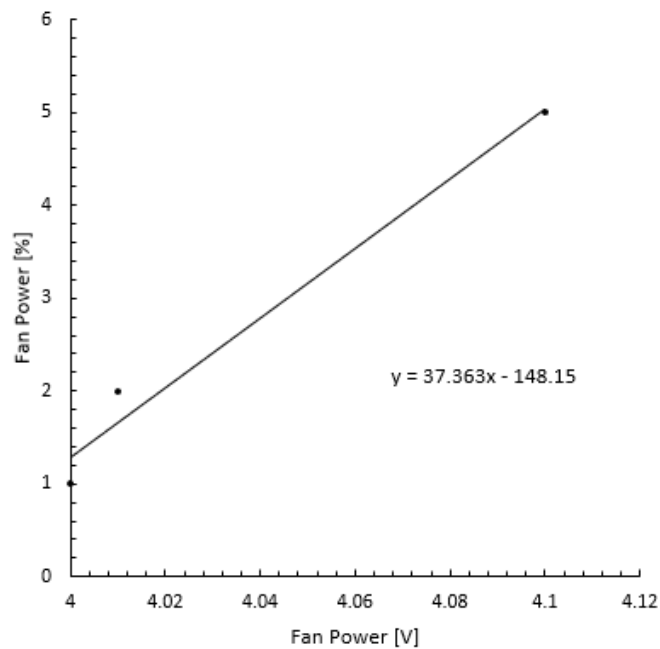


Figure 4.2: Lab fan controller voltage related to fan power, where voltage points, and therefore measured inlet velocity, were related as closely as possible to NASA measurements.

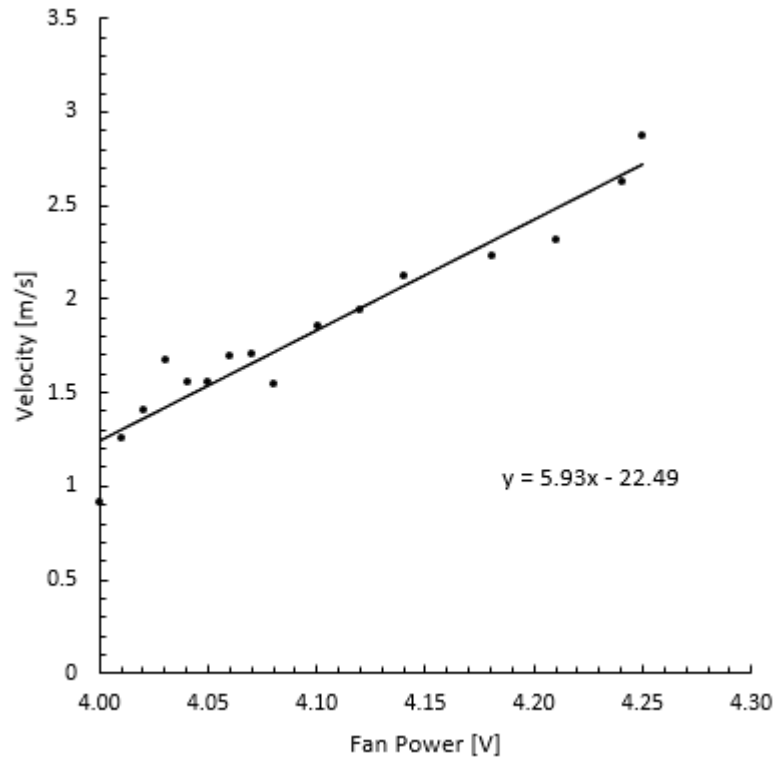


Figure 4.3: Best fit equation and region of the first regime.

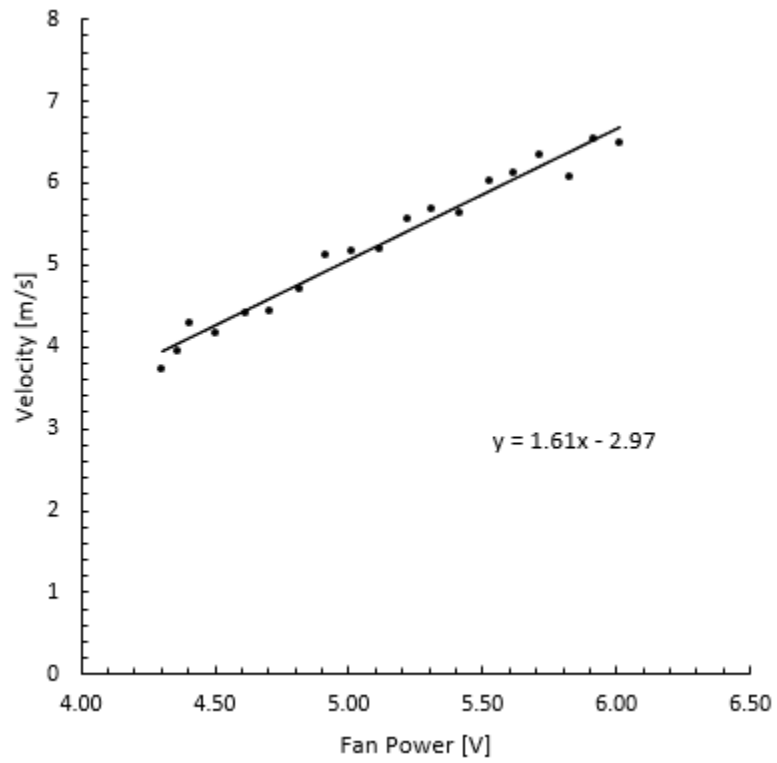


Figure 4.4: Best fit equation and region of the second regime.

in the second regime. Unfortunately, measurements up to only 5% fan power were provided, and therefore it must be assumed that this trendline is linear at least up until a fan power of 30%.

The first regime of Figure 4.1, also shown in Figure 4.3, has a trendline expressed as $Vel = 5.93V - 22.5$. When calculating the inlet velocity for a fan percentage of 10%, V , or voltage, is delegated as 4.23 V, and therefore the inlet velocity is 2.58 m/s. The second regime of Figure 4.1, also seen in Figure 4.4, has a trendline expressed as $Vel = 1.61V - 2.97$. When calculating the inlet velocity for a fan percentage of 30%, V is delegated as 4.77 V, and therefore the inlet velocity is 4.71 m/s. Table 4.3 presents the final fan percentages corresponding to their inlet velocities. The velocities presented here that were not taken from the previous calculations, which were measured with a handheld anemometer, are each related to a corresponding voltage, and were averaged over four different heights. These heights are 3.4 cm, 5 cm, 10 cm, and 12 cm above where the fuel would have been placed. This was done because the inlet velocity does in fact vary with height, so these values need to be averaged in order to be compared with the averaged NASA velocities.

Fan Percentage	1%	2%	5%	10%	30%
Voltage [V]	4.00	4.01	4.10	4.23	4.77
Corresponding Velocity [m/s]	0.918	1.27	1.86	2.58	4.71

Table 4.3: All calculated inlet velocities from the Maryland apparatus corresponding to their fan percentages.

4.2 Visual Aspects of the Fire Whirl

Each fire whirl experienced similar, but not identical, changes when transitioning from a normal gravity to a microgravity environment. Figure 4.5 presents a series of 27 frames captured from the Test 1 drop that encompasses the full visual transition the fire whirl experiences when subjected to the test conditions. The first eight frames represent the stable formation in 1- g prior to the drop. The next 19 frames represent the microgravity phase. The flame can be seen transitioning in the ninth image of the sequence. It can be clearly seen that the flame loses its elongated structure when entering the microgravity environment and never reaches the same flame heights it could in normal gravity.



Figure 4.5: Montage of selected frames from Test 1 with about 0.25 seconds between each frame.



Figure 4.6: Montage of 15 frames from Test 1 with about 0.50 seconds between each frame.

For each test, the flame length over the duration of the 5.18 second drop decreases while the flame width increases. The flames begin as a tall, slender shape, appearing as a distinguished fire whirl when buoyancy is present. Once buoyancy is removed, the flame sinks to the bottom of the enclosure and spreads out towards the enclosure edges, looking much less like a typical fire whirl. After viewing the videos captured from the cameras placed on the top and sides of the enclosure, it appears that the flames slow in rotation speed as well. This can be seen in Figure 4.6. The flame shape can be seen transitioning from a circular shape to a more dynamic shape when entering microgravity. A more dramatic view of the changes in fire whirl structure when in a normal gravity environment compared to a microgravity environment is shown in Figure 4.7.

One very interesting phenomenon occurred at the end of some drops, when

the fire whirl experiences the most g-force due to the impact of the enclosure with the deceleration cart. A partial blue whirl, as can be seen in Figure 4.8, forms for a few frames. The base of the flame appears partially blue and gradually changes to yellow the higher up the flame one views it.



Figure 4.7: Comparison of 1-*g* to 0-*g* fire whirl structure in Test 1.



Figure 4.8: Partial blue whirl formed at the end of Test 4. Occurred when the experiment vehicle reached the bottom of the drop and experienced high g-force.

4.3 Flame Height and Width

The unedited flame height and width results are presented below in Figures 4.9 through 4.15. The dotted line represents when the experiment vehicle was released.

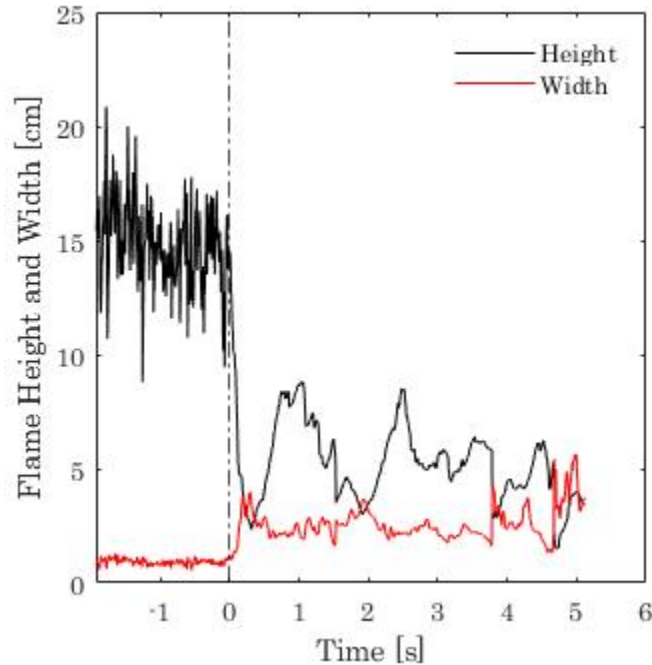


Figure 4.9: Raw height and width data for Test 1. 5% fan power, 0.476 cm gap, 1.86 m/s.

When reviewing the raw data, or Figures 4.9 through 4.15, a clear trend can be seen in the way the flame length fluctuates based on circulation (inlet wind speed). For tests with high amounts of circulation, the flame height transitions from normal gravity to microgravity in a more linear fashion, as seen in Figure 4.12. Similarly, the flame width increases slowly. Also, tests with high circulation show that instantaneous flame heights and widths fluctuate more quickly. On the other hand, data from the test with no circulation, or Test 6 seen in Figure 4.13, shows

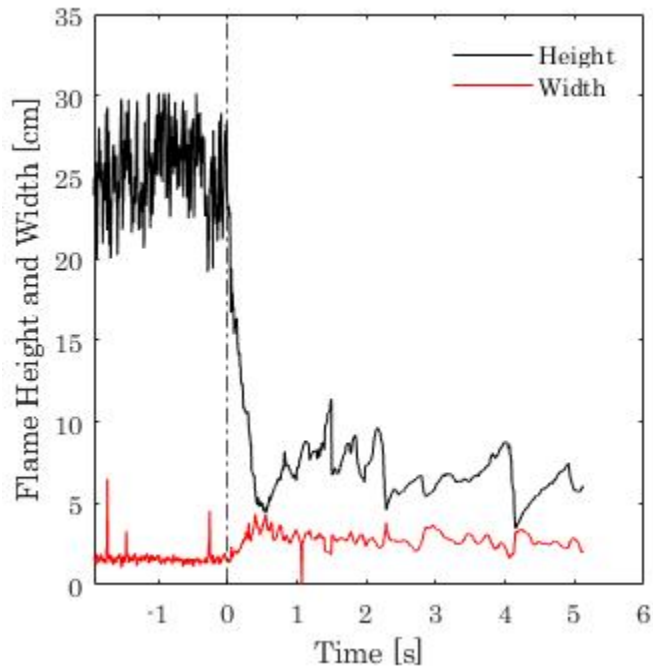


Figure 4.10: Raw height and width data for Test 2. 5% fan, 0.318 cm gap, 1.86 m/s.

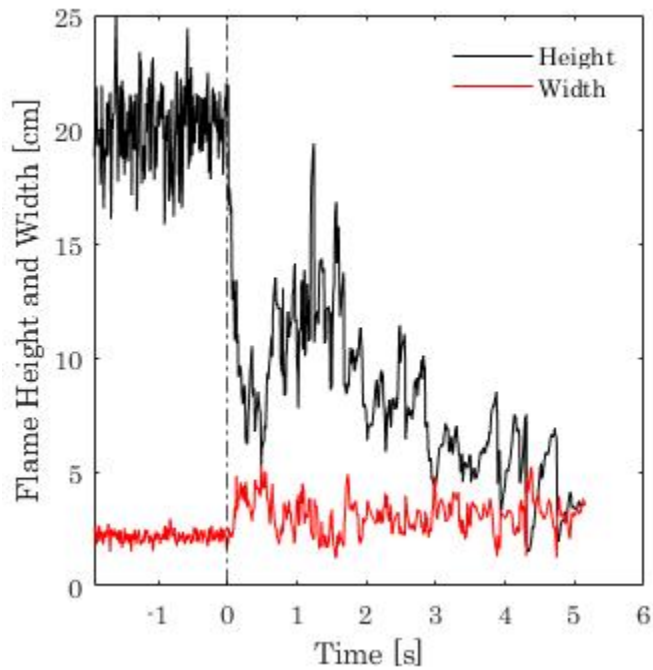


Figure 4.11: Raw height and width data for Test 4. 10% fan, 0.953 cm gap, 2.66 m/s.

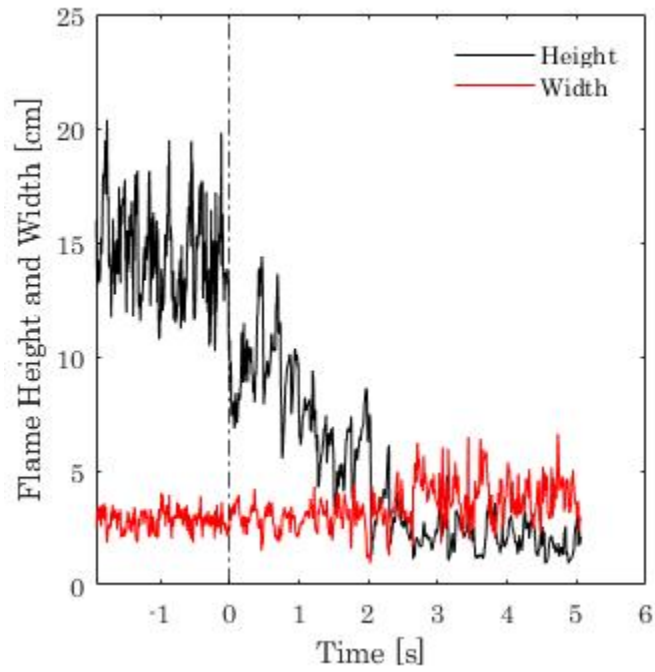


Figure 4.12: Raw height and width data for Test 5. 30% fan, 0.953 cm gap, 4.69 m/s.

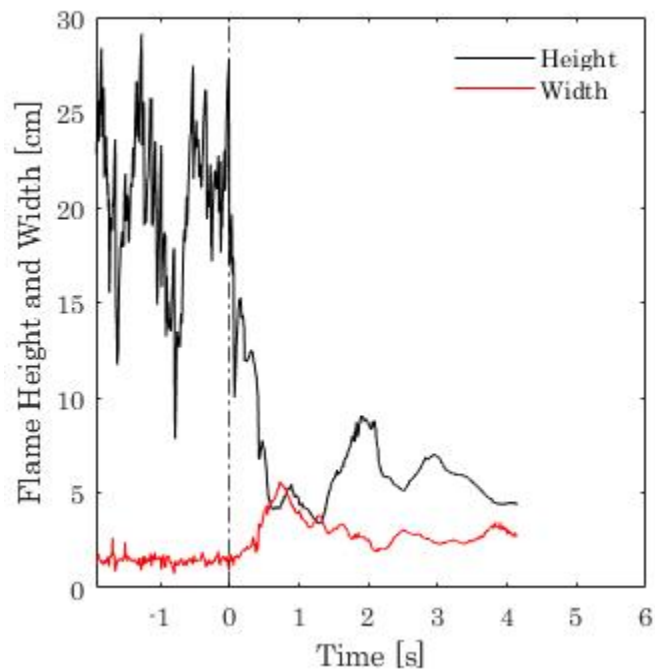


Figure 4.13: Raw height and width data for Test 6. 0% fan, 0.953 cm gap, No forced entrainment.

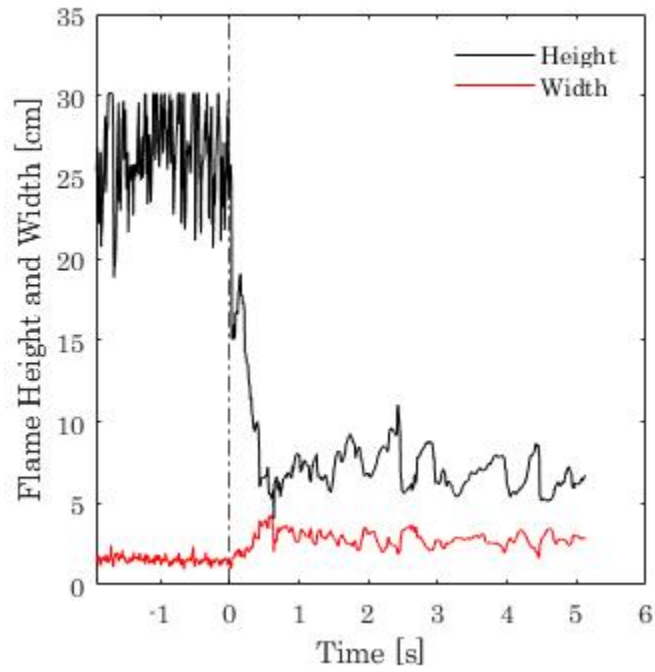


Figure 4.14: Raw height and width data for Test 7. 5% fan, 0.953 cm gap, 1.86 m/s.

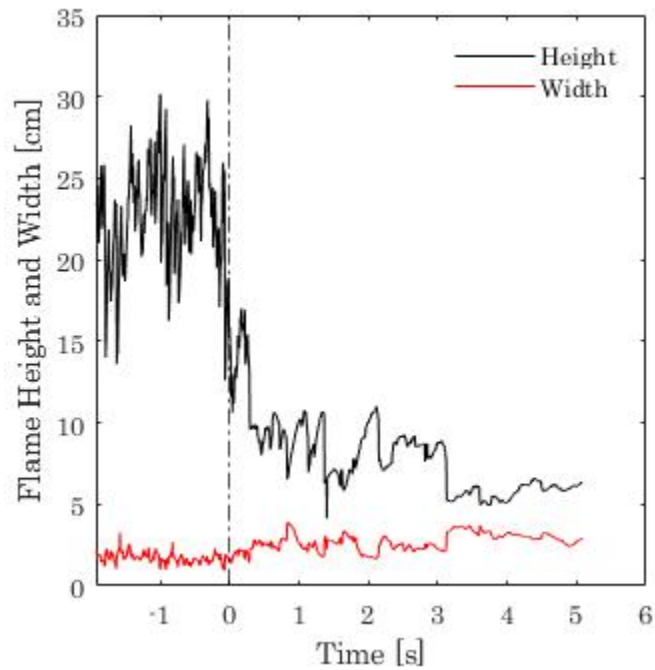


Figure 4.15: Raw height and width data for Test 9. 1% fan, 0.953 cm gap, 0.918 m/s.

a more period-like behavior, especially in terms of flame height. The flame height changes more dramatically and over a larger period of time in comparison to Test 5. Once in microgravity, the flame from Test 6 changes in terms of width and height even slower, most likely due to the lack of any kind of air flow through the test chamber.

Comparing all of the tests with the same gap size of 0.953 cm but different fan powers, a trend appears to show that as fan power is increased, there are less fluctuations in flame height and flame width. It also appears that a fan power of 5% produces the tallest flames in normal gravity conditions at this gap size, whereas the widest flames are produced from the highest fan powers.

When comparing flame heights from each of the tests with the same fan power, it appears test 2 and test 7 present similar results, while the flame height from test 1 is significantly less. Perhaps relatedly, the flame width in test 1 also reached higher values than tests 2 and 7.

4.4 Averaged Flame Height and Width

For a more quantitative view of how fire whirls change depending on fan power and gap size in microgravity, a more detailed look at the video results is important. Figure 4.16 presents the average flame heights and widths during both the 1-*g* and 0-*g* phases of each drop test with a constant inlet gap size of 0.953 cm. This includes Tests 4 through 9. The flame heights and widths are presented with respect to the fan power percentage. The error bar sizes are calculated as \pm one standard deviation

of the data.

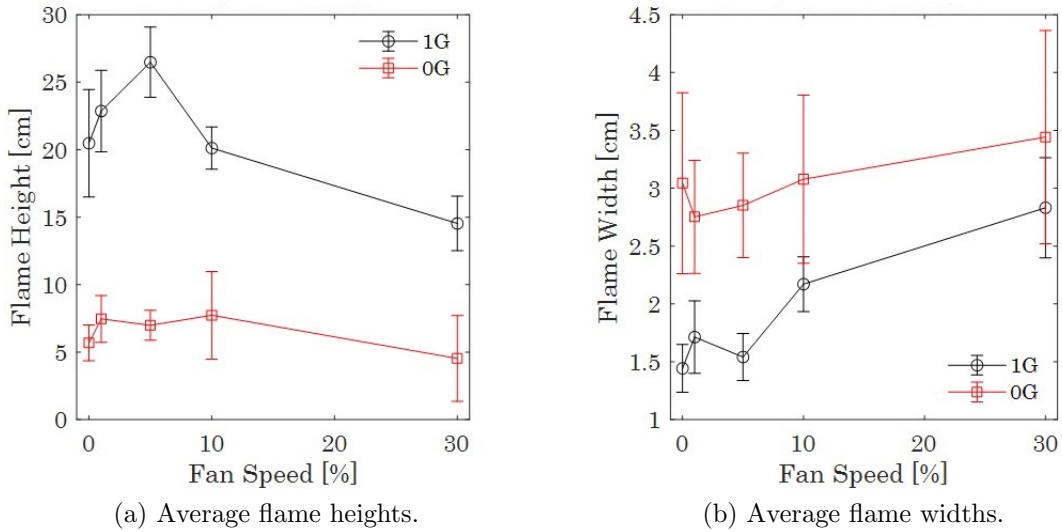


Figure 4.16: 1-*g* and 0-*g* flame heights (a) and flame widths (b) for a constant inlet gap size of 0.953 cm.

As seen above, the test condition that caused the flame to reach its tallest average height of around 26.5 cm was Test 7, with a fan power of 5%, or an inlet velocity of 1.86 m/s, and a gap size of 0.953 cm in normal gravity conditions. In a 1-*g* environment, there appears to be a clear peak in which settings lead to the tallest flame. In 0-*g*, the flame lengths appear to be less dependent on enclosure settings. Table 4.4 presents the numerical average flame heights in both 1-*g* and 0-*g* environments, respective to their test conditions. Table 4.5 presents the average numerical flame widths under the same conditions. The trend presented here suggests that there is a sweet spot to achieve maximum flame height based on inlet velocity. This trend does not seem to carry over in microgravity. Flame width follows a different trend. It would broadly appear that in both normal gravity and microgravity conditions, the largest flame width occurs at the greatest amount of circulation, or

inlet velocity. It is clear from each test that flame height always decreases and flame width always increases in microgravity.

	Test 4	Test 5	Test 6	Test 7	Test 9
Avg 1- <i>g</i> Height [cm]	20.1	14.5	20.5	26.5	22.9
Avg 0- <i>g</i> Height [cm]	7.73	4.53	5.68	6.99	7.46

Table 4.4: Averaged flame heights for all tests with the same gap size of 0.953 cm.

	Test 4	Test 5	Test 6	Test 7	Test 9
Avg 1- <i>g</i> Width [cm]	2.17	2.83	1.45	1.54	1.71
Avg 0- <i>g</i> Width [cm]	3.08	3.44	3.04	2.85	2.75

Table 4.5: Averaged flame widths for all tests with the same gap size of 0.953 cm.

Figure 4.17 presents the average flame heights and widths during both the 1-*g* and 0-*g* phases of each drop test with a constant fan power of 5% but different gap sizes. This includes Tests 1, 2, and 7.

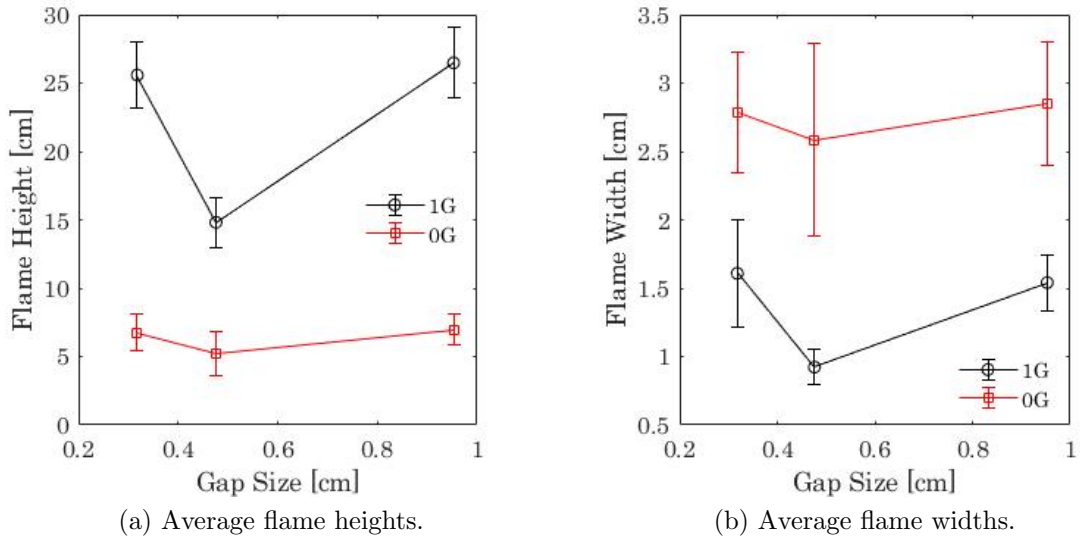


Figure 4.17: 1-*g* and 0-*g* flame heights (a) and flame widths (b) for a constant fan power of 5%.

Similarly to Figure 4.16, the graph presented above shows a more linear trend

of average values in both flame length and width when transitioned to microgravity. These tests also show similar trends, where the flame length decreases and the flame width increases in microgravity. The numerical values for each of the plotted points are presented in Tables 4.6 and 4.7.

	Test 1	Test 2	Test 7
Avg 1- <i>g</i> Height [cm]	14.8	25.6	26.5
Avg 0- <i>g</i> Height [cm]	5.21	6.77	6.99

Table 4.6: Averaged heights for all tests with the same fan power of 5%.

	Test 1	Test 2	Test 7
Avg 1- <i>g</i> Width [cm]	0.923	1.61	1.54
Avg 0- <i>g</i> Width [cm]	2.58	2.79	2.85

Table 4.7: Averaged heights for all tests with the same fan power of 5%.

A closer look at how each fire whirl changed with time in their respective tests provides a deeper understanding at what the difference in enclosure conditions entails. Figures 4.18 and 4.19 presents this data for all tests with the same gap size of 0.953 cm over the course of the 5.18 second drop time. A vertical dotted line can be seen at time zero, with the time before being negative. This is to clearly show the beginning of the enclosure drop, where the time of the drop is labeled as time 0. The data is presented as a moving average over 40 points. These graphs are also bounded to a value of one. This is done by calculating the average flame height and flame width in 1-*g* conditions. Then, the actual values are divided by the averaged 1-*g* data for the remainder of the test duration. This allows for each test, where the lengths and widths were all different values, to be compared more clearly to each other.

Like previously stated, it appears that as fan speed increases, the more linear the flame height transitions. The flames in tests with lower fan levels appear to bounce up and down more. For Figure 4.19, it can be seen that the width of the flame in the test with no fan varied by a huge amount when compared with other tests. Once again, in tests where the fan was powered to its highest, the flame width changed the least. Figures 4.20 and 4.21 presents this same data, but for all tests with the same fan speed of 5%. These values are presented as a moving average over 20 frames so that trends between tests can be seen more clearly. L_f and W_f represent the instantaneous flame length and width respectively, where L_{avg} and W_{avg} represent the averaged values. While the tests with a gap size of 0.318 cm and 0.953 cm gap size follow very similar trends, the flame height and width in the test with the middle gap size fluctuates much more, and reaches higher values in both flame height and width.

A more detailed look at one specific test, in this case Test 4, is given in Figure 4.22 to more clearly present how the drop affects a fire whirl in general. It can be seen here that once the experiment vehicle is dropped, the flame length drops and the flame width rises. The flame length, as well as the flame width, appears to fluctuate much more than before the drop.

Once again, negative time indicates the height and width values that were recorded before the drop. The values were averaged over a period of 40 frames in order to more clearly display these results, as an unedited display would appear very noisy and unclear and 20 points was not enough to provide sufficient clarity. Specifically for this test, the flame height sits around 5 cm tall at the end of the

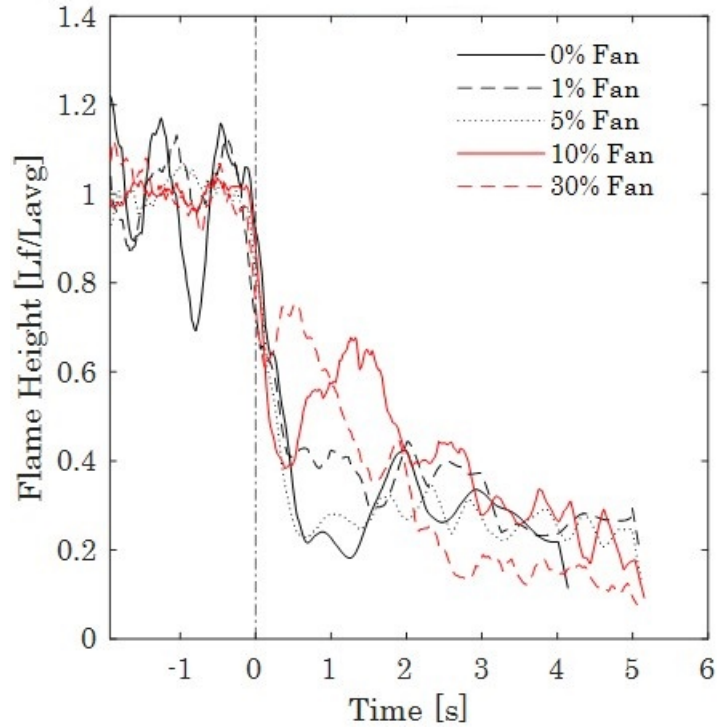


Figure 4.18: 1-*g* and 0-*g* flame heights for a constant gap size of 0.953 cm over time for a moving average of 40.

drop period, which is about 1/4th of its starting height. The width appears to grow by only about 2 cm.

4.5 Fire Whirl Rotation Analysis

The fire whirl rotation analysis was completed using Spotlight-16, a program developed that, like ImageJ, allows the user to analyze videos frame-by-frame, but also allows for different tracking methods of specified flame shapes in each frame. In each video, a trackable flame shape in the fire whirl was chosen. These trackable shapes are generally large protruding arms which are clearly defined and can be seen rotating around the center of the whirl. Table 4.8 presents the calculated rotation

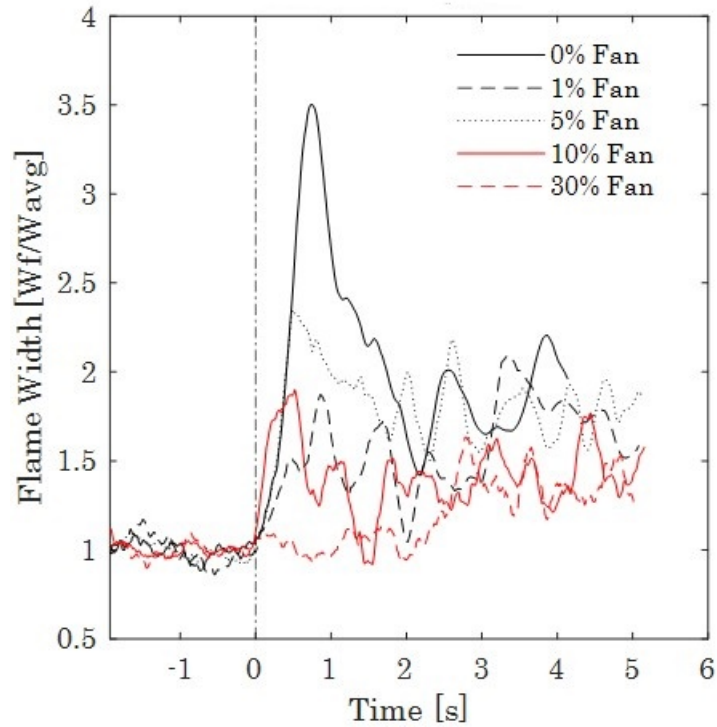


Figure 4.19: 1-*g* and 0-*g* flame heights for a constant gap size of 0.953 cm over time for a moving average of 40.

speeds for each test.

Test Number	1	2	4	5	6	7	9
Rotation Speed [cm/s]	57.8	30.1	99.8	173.9	60.4	73.6	59.9
Fan Power [%]	5	5	10	30	0	5	1
Inlet Velocity [m/s]	1.86	1.86	2.58	4.71	-	1.86	0.918

Table 4.8: Each test and their respective rotation speeds.

Each fire whirl rotation speed was calculated by using the manual tracking tool over each frame where the flame shape was present. Once this process was finished, Spotlight-16 would print out the x and y pixel coordinates for each manual click throughout the track. Then, the distance formula was used to calculate the distance traveled between each manual click. All of these distances were averaged over the course of the track. To convert this value into rotation speed, the distance

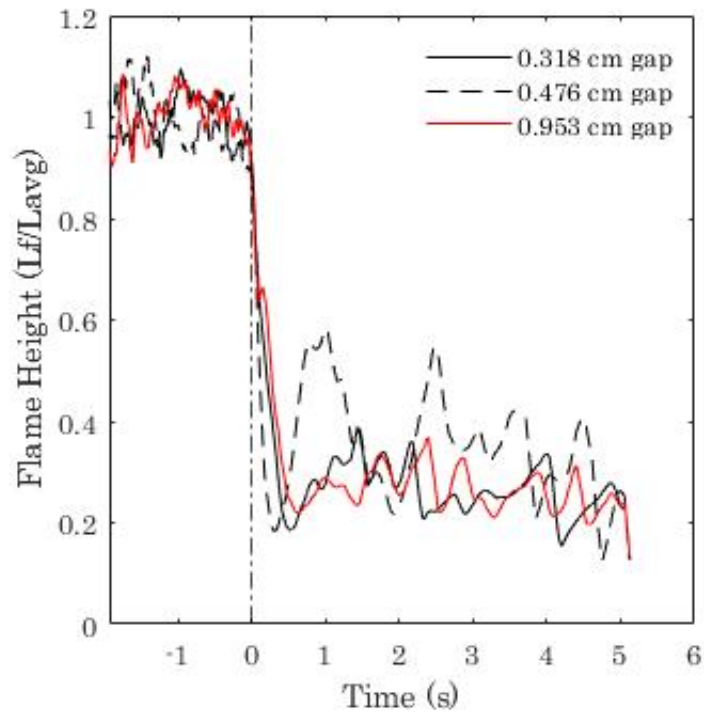


Figure 4.20: 1-*g* and 0-*g* flame heights for a constant fan power of 5% over time for a moving average of 20.

per click was divided by the ratio of pixels to cm, or 57 pixels per cm, and then multiplied by the framerate of the video. This results in a value with units of cm/s.

Figure 4.23 presents the relationship between fan power percentage and the fire whirl tangential velocity, or rotation speed. This data is presented for each test with a gap size of 0.953 cm, as to ensure the only variable changed is fan power. From the graph, it is apparent that an increase in fan power also relates to an increase in tangential velocity. Figure 4.24 presents the same relationship, though against inlet velocity rather than fan power. The condition with 0% fan power is not included as it has no forced air entrainment and the actual inlet velocity is unknown.

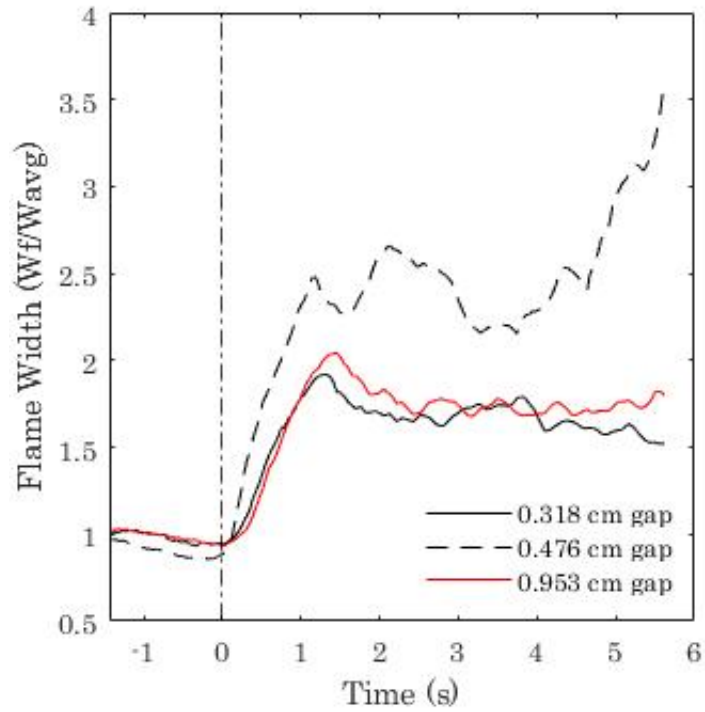


Figure 4.21: 1-*g* and 0-*g* flame widths for a constant fan power of 5% over time for a moving average of 20.

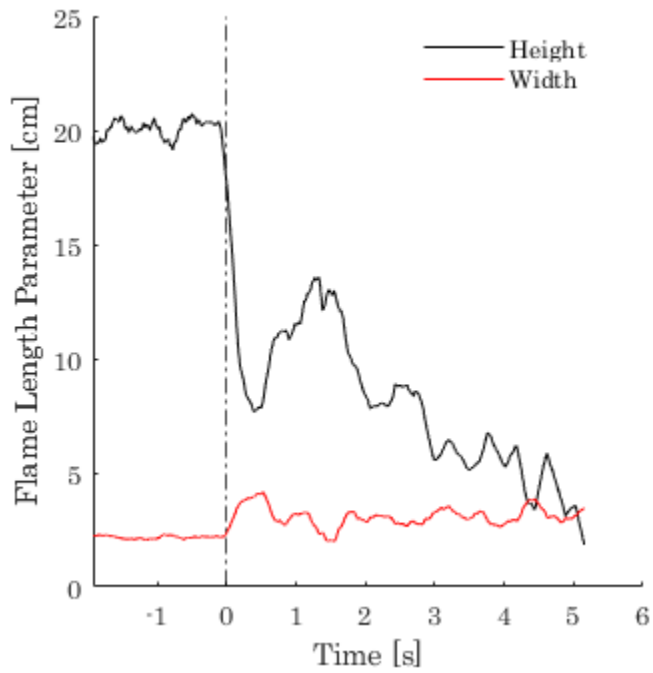


Figure 4.22: Length and width over time for Test 4 over a moving average of 40.

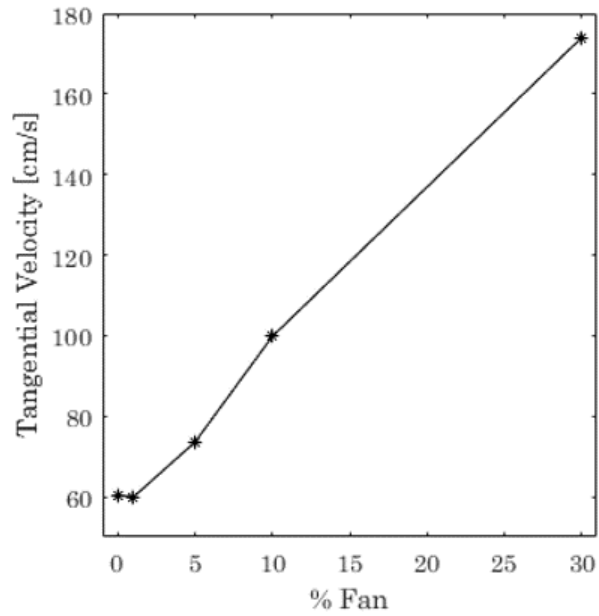


Figure 4.23: Fan power percentage plotted against fire whirl rotation speed. Every point presented is a test condition with a gap size of 0.953 cm.

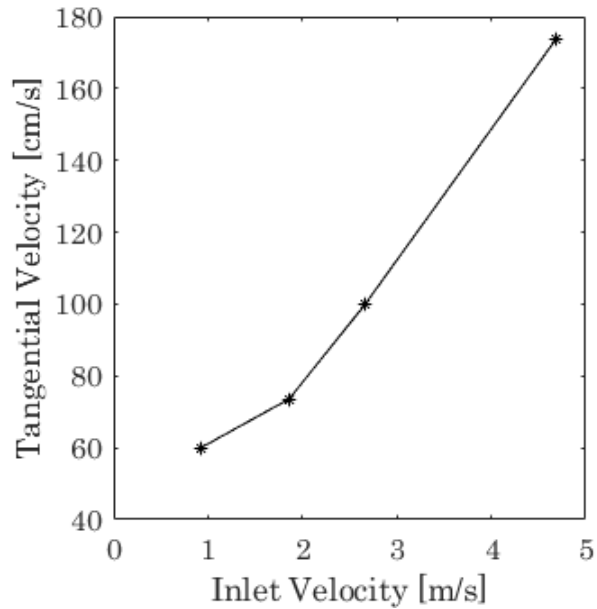


Figure 4.24: Inlet velocity plotted against fire whirl rotation speed. Every point presented is a test condition with a gap size of 0.953 cm.

Chapter 5: Discussion and Conclusions

This chapter delves into what has been learned through these seven drop tests in terms of fire whirl science. A look at future work related to these experiments is also included.

5.1 Discussion

The results suggest that as fan speed increases, increased fluctuations are observed in instantaneous flame height and width as the flame transitions from 1-g to 0-g. While an increase in variability is seen, the overall trend over time as the flame transitions from normal gravity to microgravity appears to follow a more steady and linear decay rather than the sharp and periodic decay seen as fan speed increases. A good example of a clear periodic flame progression to microgravity can be seen again in Figure 4.9. After the initial drop, the flame height goes through several cycles, growing and shrinking about three times over the test duration.

Based on the results presented, it would appear that increasing the fan power, and therefore increasing the inlet velocity, results in the tallest flame in normal gravity when it is properly balanced with buoyancy in a certain “sweet spot”. At 5% fan power, or an inlet velocity of about 1.86 m/s, the flame height reaches its peak.

This behavior has been previously observed by Lei et al. [20], who found that flame heights over a pool fire increased up to a certain tangential velocity (circulation), followed by a decay in flame height and associated widening of the core of the whirl. In microgravity conditions, fan power does not appear to influence the flame height. One might expect that in an environment with an absence of buoyancy, the introduction of more inflow into a restricted space between two cylinders would help provide some lift in lieu of buoyancy, however this is not the case here. Whether this is a universal result, that fire whirls cannot be formed without gravity, or a result specific to this design is not yet known. It is important to keep in mind that the experimental setup was not ideal, with a several centimeter zone at the base without inflow that may not have been conducive for fire whirl formation, as it has been previously shown how sensitive they are to conditions within the bottom boundary layer. Further characterization or simulation of flow patterns within the unique flow setup used would be helpful to understand these results.

It would appear that in both normal and microgravity environments, increasing fan power (wind speed) increases the average flame width within the regime studied. This again has been observed for higher-circulation fire whirls by Lei et al. [20], which decrease in flame height and increase in flame width as circulation is significantly increased beyond a region with maximum flame height. This could be due, in part, from a transition away from a defined vortex core at the center to a more distributed solid-body rotation of the flame within the chamber, as the flame spreads out across this region. In some ways, this highlights the role of buoyancy in concentrating the vortex core for fire whirls which is not present in microgravity or

very high circulation conditions.

Changing the gap size while keeping the fan power constant has led to less conclusive results. While it seems that there is no effect on flame height or width in microgravity depending on gap size, in normal gravity conditions the middle gap size produced both the shortest and thinnest flame. It is possible that there was some kind of unique issue with this test, as there are no other tests with the same conditions to verify the data against, or this specific gap size caused an issue with the inflow pattern and resulted in a weaker flame. Without further testing of the velocity profile and how this limited opening affected inlet wind speeds, further conclusions cannot be drawn.

It is clear that fire whirls both decrease in height and increase in width in microgravity compared to normal gravity, presenting similarities with high-circulation fire whirls observed in the past [20]. The absence of buoyancy results in reduced lifting mechanisms for flames, and with the lack of gravity, less vertical fluid motion is replaced by outward diffusion of flammable vapors, expanding the width of the burning region.

With regards to circulation within the experiment chamber, it would appear that as fan power is increased, the fire whirl's rotation speed increases, indicating an overall increase in velocity within the chamber as well. This is a reasonable observation, as higher fan speeds would push more and more in at a faster rate, causing air within the chamber to rotate around quicker.

The partial blue whirl formation at the end of Test 4 is also something that needs to be discussed. Once again, this unique phenomenon can be seen in Figure

4.8. This formation occurred at the moment of impact, when the experiment vehicle reached the landing zone within the drop chamber. From the previously-mentioned literature, the blue whirl can be seen, in Figure 2.9, forming under similar conditions to a fire whirl, but with smaller values of non-dimensional circulation and heat release rate. Both of these values are inversely proportional to the effect of gravity, g . When the flame experiences higher gravitational forces at impact, this g value is increased, and therefore could result in partial blue whirl formation. As the blue whirl was found to have a defined re-circulation zone, the sudden change in gravity direction may also have contributed to the formation of this unique recirculating region, encouraging the formation of a momentary blue-whirl like flame.

5.2 Conclusions

From the results of this experiment, it would seem that buoyancy should be regarded as an essential process in generating traditional fire whirls. Even with increased levels of imposed circulation, fire whirls were unable to reach heights achieved in normal gravity environments, although there may be other experimental configurations more conducive to creating fire whirls. Higher circulation led to wider fire whirls in both 1g and microgravity environments along with a higher observed tangential velocity of the flame. Higher levels of imposed circulation also added some temporary stability to the whirl, reducing fluctuations and linearizing the transition from normal to microgravity. Some of this may be due to the unique configuration tested; however, the similarity between microgravity fire whirls and

previously-studied fire whirls under very high circulation, which both resulted in low flame heights and large widths, suggest that this circulation-dominated region suppresses the effect of gravity and no longer results in a traditional long and slender “fire whirl”. Not much can be said about varying the inlet gap size. While there is a clear difference in values between the 0.476 cm gap size when compared to the others, more tests need to be completed.

5.3 Future Work

There is still much to be learned through experiments on with fire whirls in microgravity. More testing in both microgravity and normal gravity settings should be performed.

In normal gravity conditions, which is much easier to achieve and can be tested in a normal lab, mass loss rates should be taken and related to heat release rate. To do this, the shells would be placed on top of a board that would be placed on top of a mass balance with data logging capabilities. Melted wax would be placed at the center of the shells to replicate the fuel source used at the NASA drop tower. Once a stable fire whirl was formed, the mass data logger would be initiated and allowed to function until the fuel was depleted. This process would be repeated for all conditions tested at the NASA drop tower. These mass loss rates for each test would then be compared to their respective flame areas to generate a predicted heat release rate and burning rate for each fire whirl. Mass loss rates could also be performed on microgravity experiments by measuring mass before and after the

drops are completed.

The burning rate is an important factor in fire whirl scaling analysis, specifically in predicting flame height. In the future, the mass loss rate needs to be tested and collected to fully put together a scaling analysis for these whirls and compare them to whirls from other experiments. This will help to fully understand how altering the conditions mentioned in this report affect fire whirls.

Further understanding of the flow conditions within the chamber would also be useful to interpret the results presented. While inlet velocities were measured, no information is available on the flow within the chamber, in particular at the base of the fire whirl where no inlet tangential velocity is present. Further cold-flow testing or numerical modeling may help better characterize these conditions to see the impact of this effect.

Different methods for generating fire whirls in microgravity should be pursued. Placing a large fan on the top of the enclosure rather than a set of fans along the inlets would help to elongate the fire whirl and exaggerate the differences between circulation settings without buoyancy. This would also transition the vortex from a forced to a free vortex.

More testing in microgravity is needed to verify the findings detailed in this document. More testing would also allow for more conditions to be tested and will allow for a more comprehensive understanding of how fire whirls react in microgravity and the processes involved in fire whirl formation.

Bibliography

- [1] K. H. Chuah, K. Kuwana, K. Saito, and F. A. Williams. Inclined fire whirls. *Proc. Combust. Inst.*, 33:2417–2424, 2011.
- [2] K. Kuwana, K. Sekimoto, K. Saito, and F. A. Williams. Scaling fire whirls. *Fire Safety Journal*, 43:252–257, 2008.
- [3] A. Tohidi, M. J. Gollner, and H. Xiao. Fire whirls. *Annual Review of Fluid Mechanics*, 50:187–213, 2018.
- [4] G. M. Byram and R. E. Martin. Fire whirlwinds in the laboratory. *Fire Control Notes*, page 14, 1962.
- [5] H. Xiao, M. J. Gollner, and E. S. Oran. From fire whirls to blue whirls and combustion with reduced pollution. *Proc. Natl. Academy of Sciences of the U.S.A.*, 34:9457–9462, 2016.
- [6] F. Battaglia, K. B. McGrattan, R. G. Rehm, and H. R. Baum. Simulating fire whirls. *Combust. Theory Modell.*, 4:123–138, 2000.
- [7] Y. Hu, S. B. Hariharan, H. Qi, M. J. Gollner, and E. S. Oran. Conditions for formation of the blue whirl. *Combustion and Flame*, 205:147–153, 2019.
- [8] J. I. Petty. Zero-gravity plane on final flight. 2004.
- [9] K. H. Chuah and G. Kushida. The prediction of flame heights and flame shapes of small fire whirls. *Proc. Combust. Inst.*, 31:2599–2606, 2007.
- [10] J. G. Quintiere. Principles of fire behavior. *Thomas Delmar Learning*, 1998.
- [11] C. H. V. Ebert. The meteorological factor in the hamburg fire storm. *Weatherwise*, 16(2):70–75, 1963.
- [12] Forest Service and U.S. Department of Agriculture. A fire whirlwind of tornadic violence. *Fire Control Notes*, 13, 1952.

- [13] G. M. Byram and R. E. Martin. The modeling of fire whirlwinds. *Forest Science*, 16:386–399, 2003.
- [14] M. J. Pattison. Vortices. *Thermopedia*, 2011.
- [15] K. A. Hartl and A. J. Smits. Scaling of a small scale burner fire whirl. *Combustion and Flame*, 163:202–208, 2016.
- [16] J. Lei and N. Liu K. Satoh. Buoyant pool fires under imposed circulations before the formation of fire whirls. *Proc. Combust. Inst.*, 35:2503–2510, 2015.
- [17] H. W. Emmons and S. J. Ying. Fire whirl. *International Symposium on Combustion*, (11th), 1966.
- [18] J. Lei, N. Liu, L. Zhang, H. Chen, L. Shu, P. Chen, Z. Deng, J. Zhu, K. Satoh, and J. L. de Ris. Experimental research on combustion dynamics of medium-scale fire whirl. *Proc. Combust. Inst.*, 33(2):2407–2415, 2011.
- [19] S. B. Hariharan. The structure of the blue whirl: a soot-free reacting vortex phenomenon. 2017.
- [20] J. Lei and N. Liu. Reciprocal transitions between buoyant diffusion flame and fire whirl. *Combustion and Flame*, 167:463–471, 2016.
- [21] H. E. Graham. Fire whirlwinds. *Bull. Am. Meteorol. Soc.*, 36:99–103, 1955.
- [22] S. Soma and K. Saito. Reconstruction of fire whirls using scale models. *Combustion and Flame*, 86:269–284, 1991.
- [23] K. Kuwana, K. Sekimoto, K. Saito, F. A. Williams, Y. Hayashi, and H. Masuda. Can we predict the occurrence of extreme fire whirls? *AAIA J.*, 45:16–19, 2007.
- [24] P. H. Thomas. The size of flames from natural fires. *Proc. Combust. Inst.*, 9:844–859, 1963.
- [25] F. A. Williams. *Combustion theory*. 1985.
- [26] S. B. Hariharan, Y. Hu, H. Xiao, M. J. Gollner, and E. S. Oran. The structure of the blue whirl. *Annual Meeting of the APS Division of Fluid Dynamics*, (70th), 2017.
- [27] S. B. Hariharan, E. T. Sluder, M. J. Gollner, and E. S. Oran. Thermal structure of the blue whirl. *Proc. Combust. Inst.*, 37:4285–4293, 2018.
- [28] S. B. Hariharan, P. M. Anderson, H. Xiao, M. J. Gollner, and E. S. Oran. The blue whirl: boundary layer effects, temperature and oh measurements. *Combustion and Flame*, 203:352–361, 2019.
- [29] R. A. Yetter, I. Glassman, and H. C. Gabler. Asymmetric whirl combustion: a new low nox approach. *Proc. Combust. Inst.*, 28:1265–1272, 2000.

- [30] J. Lei, N. Liu, Y. Jiao, and S. Zhang. Experimental investigation on flame patterns of buoyant diffusion flame in a large range of imposed circulations. *Proc. Combust. Inst.*, 36:3149–3156, 2017.
- [31] P. D. Ronney. Premixed-gas flames. *Microgravity Combustion: Fires in Free Fall*, pages 35–82, 2001.
- [32] J. P. Downey. Microgravity materials research. *A Researcher's Guide to: International Space Station*, 2015.
- [33] H. Ross. Microgravity combustion. *Academic Press*, (1st), 2001.